

FIP-TOI: Fast Imaging Pipeline for Pulsar Localisation with a Transient-Oriented Radio Astronomical Imager

Xiaotong Li,¹ Karel Adámek,¹ Michael Giles,² and Wesley Armour^{1*}

¹*Department of Engineering Science, University of Oxford, 7 Keble Rd, Oxford OX1 3QG, UK*

²*Mathematical Institute, University of Oxford, Woodstock Rd, Oxford OX2 6GG, UK*

Accepted XXX. Received YYY; in original form ZZZ

ABSTRACT

Rapid localisation of celestial transients like pulsars requires efficient short-timescale imaging. In radio astronomy, Fast Imaging Pipeline (FIP) addresses this need by reconstructing radio astronomical images and identifying candidates statistically. The FIP comprises imaging and localisation components but conventional radio astronomical imagers, optimised for longer integrations, limit its efficiency. To overcome this limitation, a Transient-Oriented Imager (TOI) is developed based on Singular Value Decomposition (SVD) and parallelised on NVIDIA GPUs using CUDA. Integrating the TOI with an advanced transient detector, FITrig, forms the FIP-TOI enabling real-time and high-precision localisation of pulsar candidates. For $4K \times 4K$ pixel images, FIP-TOI accelerates localisation by roughly tenfold compared to a pipeline using the standard imager WSClean. Testing on diverse datasets — including fields with multiple pulsars, an on-and-off pulsar, and a pulsar exhibiting intensity changes — FIP-TOI demonstrates robust performance across all scenarios.

Key words: Radio Astronomy – Pulsar Localisation – Fast Imaging Pipeline – Transient-Oriented Imager – GPU

1 INTRODUCTION

Celestial transients, such as pulsars [Lorimer & Kramer \(2004\)](#), supernovae [Murdin & Murdin \(2011\)](#), and fast radio bursts (FRBs) [Popov et al. \(2018\)](#), are unique celestial sources characterised by significant changes over short timescales. Detecting and localising these transients often relies on snapshot surveys such as ThunderKAT [Woudt et al. \(2018\)](#), ASKAP VAST survey [Murphy et al. \(2021\)](#), realfast VLA survey [Law et al. \(2018\)](#), and Fast Imaging Pipeline (FIP) for Square Kilometre Array (SKA) [Stolyarov et al. \(2025\)](#). FIP comprises “imaging” and “localisation” components: it reconstructs images from visibilities (correlations of radio signals received by antennas) captured over short durations. These reconstructed “snapshots” images are then analysed statistically to identify potential transient candidates.

Astronomers currently employ radio astronomical imagers, such as W-Stacking Clean (WSClean; [Offringa et al. 2014](#)) and imaging tools in Common Astronomy Software Applications (CASA; [McMullin et al. 2007](#); [The CASA Team et al. 2022](#)) for the imaging component [Pelisoli et al. \(2023\)](#); [Caleb et al. \(2022\)](#). For the localisation component, source finding techniques are commonly used, such as SFIND [Hopkins et al. \(2002\)](#), AEGEAN [Hancock et al. \(2012, 2018\)](#), SORce FInding Application (SOFIA) 2 [Serra et al. \(2015\)](#); [Westmeier et al. \(2021\)](#), and FITrig [Li et al. \(2025\)](#). Among these, FITrig provides a real-time, highly sensitive, and low-false-positive approach to detect and localise transients. It produces a transient-oriented Low-Information Similarity Index (tLISI) matrix, highlighting regions likely to contain transients. These regions are

then passed to image- or image-frequency-domain source finders to precisely localise the transients’ positions.

Existing imagers can reconstruct individual snapshots of the sky; however, they lack the computational efficiency needed for transient detection, particularly in real-time analysis. The limitation becomes more pronounced with the vast data volumes that will be collected by next-generation telescopes, such as the SKA [Swart et al. \(2024\)](#)¹ and the Deep Synoptic Array (DSA) 2000².

Specifically, in radio interferometric imaging, the relationship between the observed visibility and the received sky brightness distribution (SBD; [Thompson 1999](#)) follows the van Cittert-Zernike theorem [Thompson et al. \(2017\)](#), which can be expressed as

$$Vis(u, v, w) = \iint I(l, m) e^{-i2\pi(ul+vm+w(\sqrt{1-l^2-m^2}-1))} dl dm, \quad (1)$$

where Vis is the observed visibility, I is the received SBD, u, v, w represent coordinates in the frequency domain, while $l, m, n = \sqrt{1-l^2-m^2}$ represent coordinates in the spatial domain. The w indicates the delay tracking direction, with u and v lying in the perpendicular plane.

For narrow-field imaging, the w -term is negligible, and the relationship shown in Equation (1) reduces to a two-dimensional (2-D) Fourier transform. However, for wide-field imaging, the w -term cannot be ignored due to the broad range of w . W -correction methods have been developed to address the w -term in wide-field imaging. For computational purposes, the Fast Fourier Transform (FFT) is preferred for the Fourier transform in the image reconstruction, mak-

* E-mail: wes.armour@oerc.ox.ac.uk

¹ <https://www.skao.int/en>

² <https://www.deepsynoptic.org/overview>

ing gridding a necessary step in the computation. Typically, the w -correction is integrated with the gridding step.

Imaging techniques based on the three-dimensional (3-D) Fourier transform have been proposed [Cornwell & Perley \(1992\)](#), but they are computationally intensive and impractical for real-time applications. In addition, [Perley \(1999\)](#) attempted to cover the entire field by combining multiple facets; however, this approach encounters challenges when dealing with sources that extend across facet boundaries. Moreover, w -projection method has been proposed [Cornwell et al. \(2008\)](#), which handles the entire field of view without the need for faceting. The w -projection transforms Equation (1) into a convolution of the 2-D visibility component and a \mathcal{G} component, as shown in

$$Vis(u, v, w) = Vis(u, v, w = 0) * \mathcal{G}(u, v, w), \quad (2)$$

where $\mathcal{G}(u, v, w) = \mathcal{F}\left(e^{-i2\pi(\sqrt{1-l^2-m^2}-1)w}\right)$, and \mathcal{F} indicates the Fourier operator. The w -projection approach maps all coordinates onto the $w = 0$ plane, as illustrated in Fig. 1 (a). As shown in Equation (2), the projection kernel is a function of an exponential component, which can be rewritten as sine and cosine functions using Euler's formula. As w increases, the kernel includes more oscillations, which demands finer sampling to execute the gridding process. This leads to higher costs and an increase in the computation time.

Based on these methods, hybrid algorithms such as w -snapshots have been developed. The w -snapshots method [Cornwell et al. \(2012\)](#) integrates w -projection with snapshot imaging. In this approach, visibilities collected over short timescales are gridded onto an optimal plane determined by least-square fitting. Equation (1) then transforms into

$$Vis(u, v, w) = \iint \frac{B(l', m')}{\sqrt{1-l'^2-m'^2}} e^{-i2\pi(ul'+vm')} dl' dm', \quad (3)$$

where $w = au + bv + \Delta w$, $l' = l + a\left(\sqrt{1-l^2-m^2}-1\right)$, $m' = m + b\left(\sqrt{1-l^2-m^2}-1\right)$, and a and b are parameters obtained from the least-square fitting process. All snapshots are then accumulated to produce the final reconstructed image. The w -snapshot method executes the FFT directly on the visibility plane, as illustrated in Fig. 1 (b). This approach, however, depends on the least-square fitting to define the optimal plane and requires updating after significant angular shifts in long-term observations. Moreover, as indicated in Equation (3), the visibilities are expressed in the modified coordinates l', m' . Unlike l, m , which naturally correspond to the u, v, w baseline coordinates, the transformed l', m' do not form a natural sky coordinate system. They are a mathematical artefact introduced to absorb the w -term. Additionally, this method lacks sufficient speed for the imaging in transient detection, especially during the re-projection (mapping back onto the celestial sphere) step, which depends on the World Coordinate System (WCS) package typically processed on CPUs.

Furthermore, the w -stacking method [Humphreys & Cornwell \(2011\)](#); [Offringa et al. \(2014\)](#); [Ye et al. \(2021a\)](#) has been proposed to improve performance. In this method, visibilities are gridded onto w -layers (layers of approximately constant w), with w -corrections applied following the inverse Fourier transforms. The Fourier relationship in w -stacking is expressed by

$$\frac{B(l, m)(w_{\max} - w_{\min})}{\sqrt{1-l^2-m^2}} = \int_{w_{\min}}^{w_{\max}} e^{i2\pi w(\sqrt{1-l^2-m^2}-1)} \iint Vis(u, v, w) e^{i2\pi(ul+vm)} dudvdw, \quad (4)$$

where w_{\max} and w_{\min} denote the maximum and minimum values of w , respectively. In the w -stacking method, FFTs are performed on

separate w -layers, as illustrated in Fig. 1 (c). A wide range of w values leads to a large number of layers, each requiring an FFT computation. To reduce computational demands, calculations are generally carried out on the positive w -layers, with the coordinates of negative w mapped onto the positive side. While these FFTs can be computed in parallel due to their independency, they are still computationally expensive. Additionally, w -gridding [Ye et al. \(2021b\)](#) has also been proposed to enhance both the efficiency and accuracy of the gridding process. Furthermore, ws -snapshot [Xie et al. \(2022\)](#) utilises the improved w -stacking (IW -stacking; [Ye et al. 2019](#)) combined with snapshot imaging to further boost performance.

In this article, we develop a new imager, the Transient-Oriented Imager (TOI), to improve computational efficiency and sensitivity in transient detection. TOI takes the observed visibilities as input and generates dirty snapshots, defined as the inverse Fourier transform of the observed visibilities in each sample time [The CASA Team \(2021\)](#). TOI leverages Graphics Processing Units (GPUs) to maximise computational throughput. It is then integrated with the FITrig to construct the high-performance pipeline, FIP-TOI. As the FITrig is designed to operate with dirty images, the need for deconvolution is removed from the pipeline.

This article begins with an overview of the FIP structure, as outlined in Section 2. Section 3 provides a detailed description of the development of the TOI, with a focus on its underlying mathematical principles. Section 4 discusses the GPU acceleration of the TOI and its integration with the GPU-accelerated FITrig, which completes the FIP-TOI. The performance of FIP-TOI is demonstrated in Section 5. We present our conclusions in Section 6. The GPU-accelerated TOI is open source and is available from the GitHub page³.

2 FAST IMAGING PIPELINE STRUCTURE

The conceptual diagram of FIP is shown in Fig. 2. The central images in the figure are simulated based on the GLEAM_EoR1_SKA1-Low_Generic_Set1 (GLEAM) dataset⁴⁵, generated using Oxford's Square Kilometre Array Radio-telescope simulator (OSKAR; [Dulwich et al. 2022](#)). In the simulation, a source is removed from some snapshots to represent a transient, as highlighted in the image on the right. A more detailed diagram of the FIP is presented in Fig. 3.

To make the FIP practical for widespread use among astronomers, the UVW and DATA columns (or CORRECTED_DATA, depending on user demands) from the Measurement Sets are inputted to the pipeline. Here, the UVW column indicates baselines in the UVW coordinate system, and the DATA column provides the visibilities associated with these baselines. The imager then generates a dirty snapshot for a single time sample using the corresponding UVW and DATA values.

Powered by GPUs, the TOI stores the resulting dirty snapshots directly on the device. To avoid data transfer to the host, the FITrig accesses the dirty snapshots directly on the device to produce the tLSI matrix. Candidate transients are subsequently localised within the selected regions using image- or image-frequency-domain source finders [Li et al. \(2025\)](#).

³ <https://github.com/egbdfx/SVDImager>

⁴ <https://gitlab.com/ska-telescope/sim/ska-sim-low>

⁵ <https://developer.skatelescope.org/projects/ska-sim-low/en/latest/>

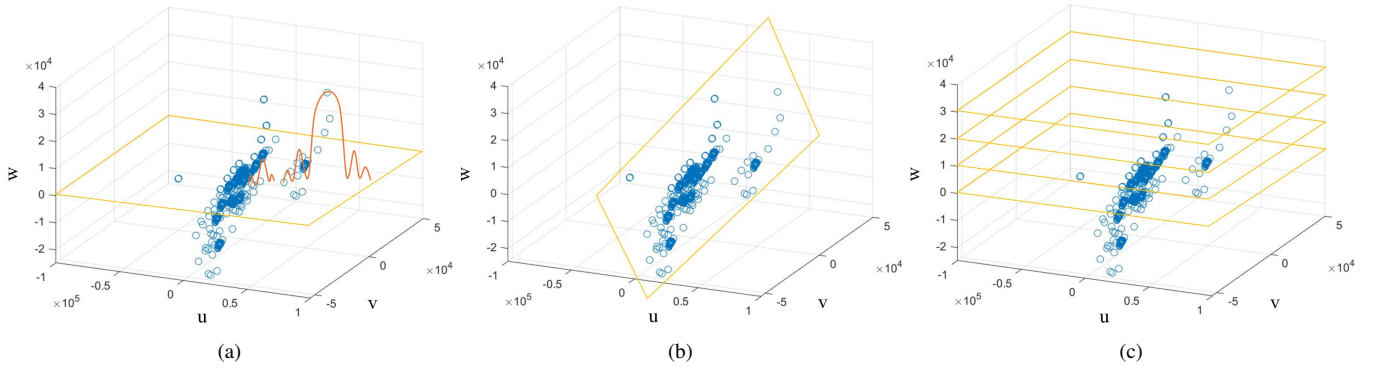


Figure 1. Planes/layers that perform FFTs in (a) w -projection, (b) w -snapshot, and (c) w -stacking methods. In (a), the kernels are schematically drawn. The blue dots represent baselines — vectors connecting the phase centres of two antennas in the radio interferometer — in the UVW coordinate systems, corresponding to a single snapshot.

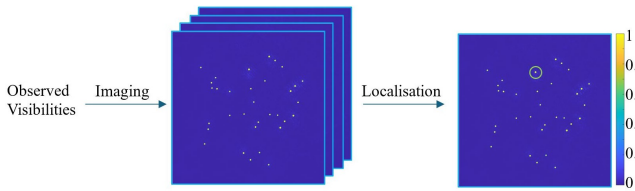


Figure 2. Conceptual diagram of the FIP. The pixel intensities are represented by the colour bar. The images are normalised in this example for illustration purposes.



Figure 3. Technical diagram of the FIP. In the diagram, UVW and DATA represent the baseline and visibility columns within the Measurement Sets.

3 TRANSIENT-ORIENTED IMAGER (TOI)

The idea driving the design of the TOI centres on the unique properties of visibilities associated with a single snapshot.

To be more precise, baselines measured within a single time sample tend to align closely with a plane in the frequency domain. This characteristic is especially relevant for next-generation telescopes, where their time resolutions are anticipated to be exceptionally fine (Kent et al. (2019); Sokolowski et al. (2024)). Given these conditions, performing the Fourier transform on planes parallel to the u, v -plane would waste computational resources. While both TOI and the w -snapshots operate on the visibility plane, TOI uses the natural 3-D coordinates from the vector-oriented formulation of the visibility equation (Burke et al. (2019)), which preserves a direct correspondence between baselines and sky directions, maintains a clear physical interpretation of the visibilities, and enhances robustness. The vector-oriented formulation is shown by

$$\text{Vis}(\mathbf{b}_\lambda) = \int A(\sigma) B_\nu(\sigma) e^{-i2\pi \mathbf{b}_\lambda \cdot \sigma} d\Omega, \quad (5)$$

where \mathbf{b}_λ represents the baseline vector in units of wavelength λ , σ indicates the source's offset vector representing its angular deviation from the phase centre, $A(\sigma)$ is the relative antenna area, B_ν denotes the sky brightness at frequency ν , and $d\Omega$ represents the angle of observation. Equation (5) illustrates that the baselines can be expressed in any coordinate system to define the visibilities. For calculating the

2-D FFT, the 3-D coordinates of baselines must first be projected to a lower dimension.

3.1 Coordinate transformation in the frequency domain

The baseline vectors (u, v, w) are approximately coplanar, which allows a reduction in dimensionality. Note that finite dump times introduce small deviations from a perfect plane, so the baselines are only nearly coplanar in practice. As demonstrated in Section 5.3, TOI performs robustly for 8s dumps, indicating that this coplanar approximation is valid for most transient detection scenarios. To reduce the dimensionality, we start by determining a 3×3 orthogonal matrix \mathbf{V} . The matrix \mathbf{V} is structured with unit vectors as its rows and columns, ensuring orthogonality, such that

$$\begin{aligned} [\mathbf{u} \ \mathbf{v} \ \mathbf{w}] &= [\mathbf{r}_1 \ \mathbf{r}_2 \ \mathbf{r}_3] \begin{bmatrix} V_{11} & V_{12} & V_{13} \\ V_{21} & V_{22} & V_{23} \\ V_{31} & V_{32} & V_{33} \end{bmatrix} \\ &= [\mathbf{r}_1 \ \mathbf{r}_2 \ \mathbf{0}] \begin{bmatrix} V_{11} & V_{12} & V_{13} \\ V_{21} & V_{22} & V_{23} \\ V_{31} & V_{32} & V_{33} \end{bmatrix} = [\mathbf{r}_1 \ \mathbf{r}_2 \ \mathbf{0}] \mathbf{V}. \end{aligned} \quad (6)$$

In Equation (6), the baseline matrix $[\mathbf{u}, \mathbf{v}, \mathbf{w}]$ represents baselines in the UVW coordinate system, with each row corresponding to a baseline and columns $\mathbf{u}, \mathbf{v}, \mathbf{w}$ as one-dimensional (1-D) arrays of coordinates. In contrast, the transformed baseline matrix $\mathbf{R} = [\mathbf{r}_1, \mathbf{r}_2, \mathbf{r}_3]$ expresses these baselines in R1R2R3 coordinate system, where each row of \mathbf{R} denotes a baseline, with $\mathbf{r}_1, \mathbf{r}_2, \mathbf{r}_3$ being 1-D arrays. The R1R2R3 coordinate system is orthogonal and right-handed, with its origin situated on the visibility plane for the given time sample. Both the r_1 - and r_2 -axes lie on this plane, while the r_3 -axis is perpendicular to it. Due to the co-planar property of the snapshot baselines, the r_3 components are zero in the baseline representations.

The data reduction matrix \mathbf{V} in Equation (6) is obtained by performing SVD on the centred baseline matrix, which has dimensions $\beta \times 3$. It is represented as

$$[\mathbf{u} \ \mathbf{v} \ \mathbf{w}] - [\gamma_1 \ \gamma_2 \ \gamma_3] \stackrel{\text{SVD}}{=} \mathbf{Q} \mathbf{D} \mathbf{P}^T, \quad (7)$$

where \mathbf{Q}, \mathbf{D} , and \mathbf{P} have dimensions $\beta \times 3, 3 \times 3$, and 3×3 , respectively. Here, $\mathbf{\Gamma} = [\gamma_1, \gamma_2, \gamma_3]$ denotes the $\beta \times 3$ mean matrix, where each 1-D array γ_i (for $i = 1, 2, 3$) consists of identical entries equal to the mean of the i -th column in the baseline matrix.

In line with principal component analysis (PCA), the columns corresponding to the top $k = 2$ principal components of matrices

\mathbf{Q} and \mathbf{P} are selected (since the baselines effectively lie in a 2-D subspace due to coplanarity), producing \mathbf{Q}_k (of size $\beta \times 2$) and \mathbf{P}_k (of size 3×2). The top-left 2×2 sub-matrix of matrix \mathbf{D} is extracted to create \mathbf{D}_k . Consequently, we define $\mathbf{V}_k = \mathbf{P}_k^T$, where \mathbf{V}_k has dimensions 2×3 . The first two rows of the matrix \mathbf{V} are set to match \mathbf{V}_k , while the third row is derived by taking the cross product of the first two rows. This construction ensures that \mathbf{V} fulfils Equation (6).

Subsequently, to obtain $[\mathbf{r}_1 \ \mathbf{r}_2]$, it is necessary to shift the matrix centre back so that it realigns with the centre of the baseline matrix, as shown by

$$[\mathbf{r}_1 \ \mathbf{r}_2] = \mathbf{Q}_k \mathbf{D}_k + \Gamma \mathbf{V}_k^T. \quad (8)$$

With this step, the process of transforming coordinates in the frequency domain, as expressed in Equation (6), is finalised.

3.2 Coordinate transformation in the spatial domain

To carry out the Fourier transform in the r_1, r_2 -plane, it is essential to transform the spatial domain coordinates appropriately. This requires constructing a matrix \mathbf{T} , such that

$$\begin{bmatrix} \mathbf{l} \\ \mathbf{m} \\ \mathbf{n} - \mathbf{l} \end{bmatrix} = \begin{bmatrix} V_{11} & V_{21} & V_{31} \\ V_{12} & V_{22} & V_{32} \\ V_{13} & V_{23} & V_{33} \end{bmatrix} \begin{bmatrix} \mathbf{t}_1 \\ \mathbf{t}_2 \\ \mathbf{t}_3 \end{bmatrix} = \begin{bmatrix} V_{11} & V_{21} & V_{31} \\ V_{12} & V_{22} & V_{32} \\ V_{13} & V_{23} & V_{33} \end{bmatrix} \mathbf{T}, \quad (9)$$

where $\mathbf{l}, \mathbf{m}, \mathbf{n}$ are 1-D row vectors with elements satisfying the relationship $n = \sqrt{1 - l^2 - m^2}$. The matrix \mathbf{T} is composed of the 1-D row vectors $\mathbf{t}_1, \mathbf{t}_2$, and \mathbf{t}_3 . Just as (u, v, w) and (l, m, n) are used to represent frequency and spatial coordinates in the standard system, \mathbf{R} and \mathbf{T} serve as the frequency and spatial coordinates in the new transformed coordinate system.

Using Equations (6) and (9), the argument of the exponential term in Equation (1) can be rewritten as

$$\begin{aligned} ul + vm + w(\sqrt{1 - l^2 - m^2} - 1) &= [u \ v \ w] \begin{bmatrix} l \\ m \\ n - 1 \end{bmatrix} \\ &= [r_1 \ r_2 \ 0] \begin{bmatrix} V_{11} & V_{12} & V_{13} \\ V_{21} & V_{22} & V_{23} \\ V_{31} & V_{32} & V_{33} \end{bmatrix} \begin{bmatrix} V_{11} & V_{21} & V_{31} \\ V_{12} & V_{22} & V_{32} \\ V_{13} & V_{23} & V_{33} \end{bmatrix} \begin{bmatrix} t_1 \\ t_2 \\ t_3 \end{bmatrix} \\ &= [r_1 \ r_2 \ 0] \begin{bmatrix} 1 & 0 & 0 \\ 0 & 1 & 0 \\ 0 & 0 & 1 \end{bmatrix} \begin{bmatrix} t_1 \\ t_2 \\ t_3 \end{bmatrix} = [r_1 \ r_2 \ 0] \begin{bmatrix} t_1 \\ t_2 \\ t_3 \end{bmatrix} = r_1 t_1 + r_2 t_2. \end{aligned} \quad (10)$$

To convert l, m to t_1, t_2 in the differential part of Equation (1), a Jacobian correction factor must be introduced. Due to the near co-planar feature, setting $t_3 = 0$ is valid and does not affect the coordinate transformation described as Equation (10). Consequently, the differential part transforms as

$$dldm = \left| \frac{\partial(l, m)}{\partial(t_1, t_2)} \right| dt_1 dt_2 = (V_{11}V_{22} - V_{21}V_{12}) dt_1 dt_2, \quad (11)$$

where scaling factor $(V_{11}V_{22} - V_{21}V_{12})$ is applied to the visibilities before performing the inverse Fourier transform.

At this stage, by substituting Equations (10) and (11) into Equation (1), we arrive at

$$\begin{aligned} \text{Vis}(u(r_1, r_2), v(r_1, r_2), w(r_1, r_2)) &= \iint I(l(t_1, t_2), m(t_1, t_2)) \\ &\quad \times e^{-i2\pi(r_1 t_1 + r_2 t_2)} \times (V_{11}V_{22} - V_{21}V_{12}) dt_1 dt_2. \end{aligned} \quad (12)$$

For implementing Equation (12), the term $(u(r_1, r_2), v(r_1, r_2), w(r_1, r_2))$ can be achieved by applying

SVD-based PCA to the baseline matrix. Furthermore, the expression $e^{-i2\pi(r_1 t_1 + r_2 t_2)} dt_1 dt_2$ indicates that the relationship between r_1, r_2 and t_1, t_2 is a Fourier transform. Only a single Fourier transform is required for each snapshot because of the near co-planar feature. Lastly, $(l(t_1, t_2), m(t_1, t_2))$ can be obtained using the relationship expressed in Equation (9).

3.3 Re-projection process

As outlined in WCS ⁶ Calabretta, M. R. & Greisen, E. W. (2002), SIN projection is employed during the re-projection process. This projection is particularly suitable for aperture synthesis in radio astronomy.

The re-projection process begins by mapping pixel coordinates (p_1, p_2) to intermediate coordinates (x, y) . Here, (p_1, p_2) corresponds to the pixel indices within the image I , which lies on a plane parallel to the t_1, t_2 -plane. This transformation is achieved by

$$\begin{cases} x = -\frac{\pi}{180} \alpha \left(p_1 - \left(\frac{N}{2} + 1 \right) \right) \\ y = \frac{\pi}{180} \alpha \left(p_2 - \left(\frac{N}{2} + 1 \right) \right) \end{cases}, \quad (13)$$

where the image consists of $N \times N$ pixels, and the size of each pixel (cell size) is α , expressed in degrees.

Next, the coordinates (x, y) are converted into native spherical coordinates (ϕ, θ) . The value of ϕ is given by

$$\phi = \begin{cases} 0, & x = 0 \text{ and } y \leq 0 \\ 180, & x = 0 \text{ and } y > 0 \\ 90, & y = 0 \text{ and } x > 0 \\ -90, & y = 0 \text{ and } x < 0 \\ \frac{180}{\pi} \text{atan2}(x, -y), & \text{otherwise} \end{cases} \quad (14)$$

The value of θ depends on the condition of $x^2 + y^2$. For $x^2 + y^2 < 0.5$, θ is calculated as

$$\theta = \begin{cases} 0, & \sqrt{x^2 + y^2} \geq 1 \text{ and } \sqrt{x^2 + y^2} - 1 < \epsilon \\ 90, & \sqrt{x^2 + y^2} = 0 \\ 180, & \sqrt{x^2 + y^2} \leq -1 \text{ and } \sqrt{x^2 + y^2} + 1 > -\epsilon \\ \frac{180}{\pi} \arccos(\sqrt{x^2 + y^2}), & \text{otherwise} \end{cases}; \quad (15)$$

for $0.5 \leq x^2 + y^2 \leq 1$, θ is determined using

$$\theta = \begin{cases} -90, & \sqrt{1 - (x^2 + y^2)} \leq -1 \text{ and } \sqrt{1 - (x^2 + y^2)} + 1 > -\epsilon \\ 0, & \sqrt{1 - (x^2 + y^2)} = 0 \\ 90, & \sqrt{1 - (x^2 + y^2)} \geq 1 \text{ and } \sqrt{1 - (x^2 + y^2)} - 1 < \epsilon \\ \frac{180}{\pi} \arcsin(\sqrt{1 - (x^2 + y^2)}), & \text{otherwise} \end{cases} \quad (16)$$

where $\epsilon = 10^{-10}$ Calabretta, M. R. & Greisen, E. W. (2002).

The third step involves transforming (ϕ, θ) back to (x, y) , while accounting for the tilt angles ξ and η of the t_1, t_2 -plane relative to the l, m -plane, where

$$\begin{cases} \xi = \frac{V_{31}}{V_{33}} \\ \eta = \frac{V_{32}}{V_{33}} \end{cases} \quad (17)$$

The conversion is defined by

$$\begin{cases} x = \frac{180}{\pi} (\cos \theta \sin \phi + \xi (1 - \sin \theta)) \\ y = -\frac{180}{\pi} (\cos \theta \cos \phi - \eta (1 - \sin \theta)) \end{cases}. \quad (18)$$

Finally, (x, y) is mapped to pixel coordinates (p'_1, p'_2) on the image

⁶ <https://github.com/Punzo/wcslib/blob/master/C/prj.c>

plane, which is parallel to the l, m -plane. This step is performed using

$$\begin{cases} p'_1 = -\frac{x}{\alpha} + \frac{N}{2} + 1 \\ p'_2 = \frac{y}{\alpha} + \frac{N}{2} + 1 \end{cases} \quad (19)$$

At this stage, the dirty image has been fully re-projected onto the celestial sphere and mapped onto the standard image plane, making it ready for users to incorporate into their data processing pipelines.

Notably, the imager we designed begins with the visibilities in the UVW coordinate system, as Measurement Sets collected by astronomers are typically represented in this system. This design ensures that the imager remains portable and accessible to a broad range of users. Alternatively, one could transform the coordinates of the measured baselines in the Measurement Set before initiating imaging from Equation (5).

4 GPU ACCELERATION

TOI leverages GPU acceleration using Compute Unified Device Architecture (CUDA; Kirk 2007), as illustrated in Fig. A1. The gridding functionality of this imager is implemented based on the SKA Science Data Processor (SDP) Processing Function Library (PFL)⁷.

TOI starts with obtaining the UVW (baselines) and DATA (visibilities) columns from the Measurement Set using the `getcol` function provided by CASACORE⁸. The PCA process based on SVD can use either the `pca` function from the Scikit-Learn library or our GPU-accelerated SVD based on the NVIDIA cuSOLVER library, which is released in the GPU-accelerated Singular Value Thresholding (SVT) software package⁹ Li et al. (2023).

To optimise the implementation, we employ a multi-streaming strategy. The re-projection process, being independent of other tasks, is assigned to Stream 2, where the coordinate transformation is performed. Meanwhile, the most computationally intensive task, the iFFT, is handled in Stream 1, using the single-precision `cufftExecC2C` function from the CUDA Fast Fourier Transform (cuFFT) library¹⁰. We use `cudaEventRecord` at the end of Stream 2 to signal its completion and control Stream 1 to wait for Stream 2's completion using `cudaStreamWaitEvent`, after which the workflow transitions to the final kernel. Within a single CUDA stream, kernels execute sequentially, with automatic synchronisation managed by the CUDA runtime. In addition, `atomicAdd` is used to ensure correctness when threads need to update the same memory location simultaneously.

For further performance enhancement, we enable `fastmath` optimisations for floating-point operations, leveraging its efficiency for the trigonometric calculations used in the TOI. Notably, TOI utilises custom-developed functions written according to the mathematical principles detailed in Section 3. By eliminating dependencies on external libraries like Nifty Gridding Selig et al. (2013) and WCSLIB Calabretta, M. R. & Greisen, E. W. (2002); Greisen, E. W. & Calabretta, M. R. (2002), this design enhances the pipeline's flexibility and portability.

TOI generates a dirty snapshot for data (UVW and DATA) in each time sample, which is then used by the FITrig for subsequent transient localisation. The most essential component in the FITrig is

the calculation of tLISI, as expressed by

$$\begin{aligned} \text{tLISI}_t^{(s)} \left(\mathbf{D}_t^{(s)}, \mathbf{D}_t^{(s+1)}, \mathbf{x}_t^{(s+1)} \right) \\ = 1 - \frac{\text{mean} \left(\left| \mathbf{D}_t^{(s)} - \mathbf{D}_t^{(s+1)} \right| \right) \max \left(\left| \mathbf{D}_t^{(s)} - \mathbf{D}_t^{(s+1)} \right| \right) \text{mean} \left(\mathbf{r}_t^{(s)} \right)}{\max \left(\max_{s=1}^L \mathbf{x}^{(s)}, C \right) \max \left(\max_{s=1}^L \mathbf{x}^{(s)}, C \right)}. \end{aligned} \quad (20)$$

In the FITrig, images are divided into multiple tiles, and the rate of change for each tile is determined by comparing consecutive dirty snapshots to localise potential transient events. In Equation (20), t indicates tile index, L indicates the total number of snapshots in the time-sequential measurement, $s = 1, 2, \dots, L - 2$ indicates snapshot index, \mathbf{x} indicates a snapshot, \mathbf{D} is the difference image between adjacent snapshots, \mathbf{r} indicates a ratio matrix representing the importance of change, and $C = 10^{-6}$ is a constant to avoid instability. A tLISI value is output for each tile. The lower the tLISI value, the more likely the tile contains transient events. Accelerated by GPUs, the functional diagram of the tLISI kernel is shown in Fig. A2. A comprehensive presentation of tLISI and our FITrig is presented in Li et al. 2025.

5 PERFORMANCE

This section presents experiments designed to assess the performance of the FIP-TOI, which integrates the TOI with the FITrig, in comparison to a WSClean-based pipeline that utilises WSClean (w -stacking gridding) along with the FITrig. The analysis focuses on the TOI's performance relative to WSClean, since it is widely adopted among astronomers for transient discovery Pelisoli et al. (2023); Caleb et al. (2022).

To evaluate the image quality of the TOI, we apply the imager to datasets simulated by OSKAR, using telescope configurations from SKA1-LOW, SKA AA2 (from SKA1-MID), and MeerKAT. Next, the computational efficiency of the FIP-TOI is evaluated against that of the WSClean-based pipeline. Finally, to highlight the versatility of the FIP-TOI across various datasets, we apply the pipeline to observation-based Measurement Sets of GLEAM, PSR J0901-4046 Caleb et al. (2022), and PSR J1703-4902 Driessen et al. (2022); Tremou et al. (2020).

5.1 Image quality

For this study, we simulate SBDs using OSKAR. The field of view (FOV) is set to a wide field of 3 degrees. Within this FOV, 16 sources are arranged in a 4×4 grid, evenly distributed with each spacing in both horizontal and vertical directions. This uniform distribution spans the entire image, enabling an impartial assessment of the TOI's performance across all image regions. The same SBD is simulated using various telescope configurations to avoid bias. Here, we utilise the layouts of SKA1-LOW, SKA AA2 (MID), and MeerKAT telescopes. In the experiment, SKA1-LOW functions at a lower frequency of 60 MHz, whereas both SKA AA2 (from SKA1-MID) and MeerKAT function at a higher frequency of 1.2 GHz. The dirty snapshots produced by the WSClean and TOI are illustrated in Fig. 4. These images have dimensions of 4096×4096 pixels (denoted as $4K \times 4K$ pixels), with each pixel corresponding to a cell size of 0.0007334 degrees.

Among various Image Quality Assessment (IQA) methods, the augmented Low-Information Similarity Index (augLISI) Li et al. (2024b) has been specifically designed to evaluate radio astronomical

⁷ <https://gitlab.com/ska-telescope/sdp/ska-sdp-func>

⁸ <https://casacore.github.io/casacore/>

⁹ <https://github.com/egbdfx/gpuSVT>

¹⁰ <https://docs.nvidia.com/cuda/cufft/>

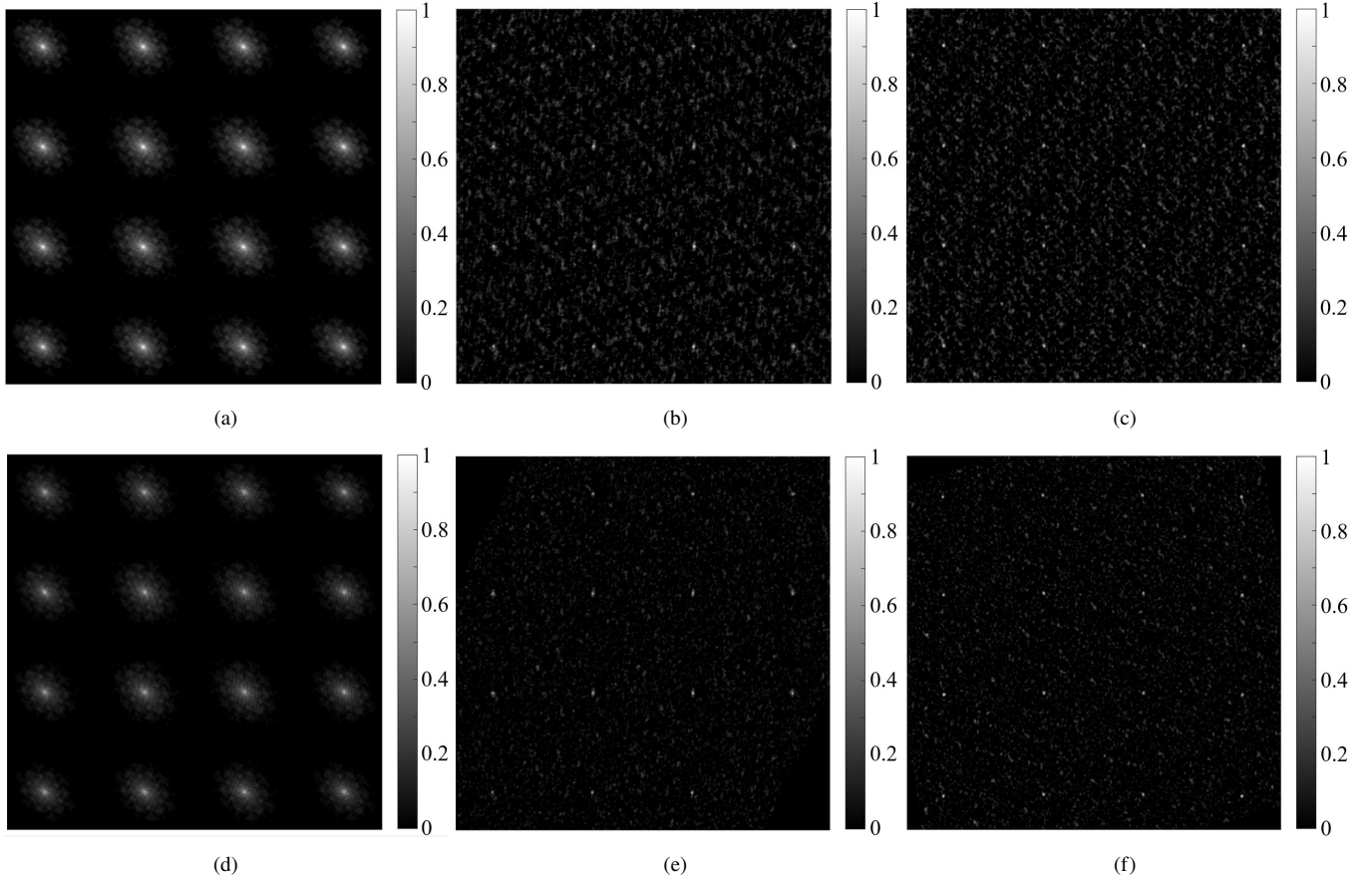


Figure 4. Dirty snapshots generated by (top row) WSClean and (bottom row) TOI using (left column) SKA1-LOW, (middle column) SKA AA2, and (right column) MeerKAT telescope layout. The images are illustrated with comparable intensity scales.

Table 1. IQA and noise evaluation for WSClean and TOI images.

| Telescope Layout | augLISI | Noise (WSClean) | Noise (TOI) |
|------------------|---------|-----------------|-------------|
| SKA1-LOW | 0.9821 | 0.0465 | 0.0330 |
| SKA AA2 (MID) | 0.9596 | 0.0565 | 0.0349 |
| MeerKAT | 0.9275 | 0.0592 | 0.0408 |

images, particularly those with extended source structures or high noise levels. Since we are working with dirty images here, we adopt augLISI to evaluate their similarities. We use augLISI to compare the images produced by WSClean and TOI, obtaining a similarity score between 0 and 1, where higher values indicate that the celestial sources in the two images are more similar and lower values indicate greater differences. On the other hand, the noise level is estimated by computing the standard deviation of pixel intensities in a featureless crop of each normalised image; the higher value indicates the noisier image. The IQA results, including the noise evaluation, are shown in Table 1.

The results show that the augLISI values are approaching 1, suggesting a high similarity between the sources in each comparison. Moreover, the noise evaluation reveals that the Point Spread Function (PSF) side lobes and noise are less intense in the TOI's outputs than in those produced by WSClean. This result is consistent with visual inspection, providing quantitative confirmation that the TOI correctly reconstructs the sources.

Admittedly, TOI has a limitation, where in the FOV, the corners

may be absent in the reconstructed image. For instance, the bottom-right and the top-left corners are missing in Fig. 4 (e), as evident from both tile-wise image quality assessment Li et al. (2024b,a) and visual inspection. This issue primarily occurs from the transformation between the t_1, t_2 -coordinates and the l, m -coordinates, during which the image undergoes a rotation, as expressed by Equation (9). While the re-projection process contributes to this rotation, the primary cause is the coordinate transformation itself. The proportion of missing pixels is determined by the angle between t_1, t_2 - and l, m -planes.

To quantitatively assess the impact of missing corners, we computed the ratio of the effective region within each image. This task can be achieved by finding the proportion of the intersection area between two parallelograms ($A \cap B$) relative to the area of the parallelogram B. The centres of both parallelograms are set at the origin (0, 0) of the Cartesian coordinate system. The vertices of parallelogram A are defined by

$$\left(\frac{V_{21} - V_{11}}{V_{33}}, \frac{V_{22} - V_{12}}{V_{33}} \right), \left(-\frac{V_{11} + V_{21}}{V_{33}}, -\frac{V_{22} + V_{12}}{V_{33}} \right),$$

$$\left(\frac{V_{11} + V_{21}}{V_{33}}, \frac{V_{12} + V_{22}}{V_{33}} \right), \left(\frac{V_{11} - V_{21}}{V_{33}}, \frac{V_{12} - V_{22}}{V_{33}} \right).$$

Meanwhile, the vertices of parallelogram B are given by

$$(1, 1), (1, -1), (-1, 1), (-1, -1).$$

These equations reveal that the rotation is symmetric about the image

Table 2. The ranges (shown by maximum and minimum values) of ρ for different step sizes κ .

| κ | $\max(\rho)$ | $\min(\rho)$ |
|----------|--------------|--------------|
| 0.1 | 0.9917 | 0.9184 |
| 0.01 | 1.0000 | 0.9151 |
| 0.001 | 1.0000 | 0.9143 |
| 0.0001 | 1.0000 | 0.9142 |

centre, which allows us to focus on a single direction to estimate the ratio. Using algebraic methods and considering the direction shown in Fig. 4 (e), the area excluded from parallelogram B can be expressed as

$$-\frac{(1 - V_{11} + V_{12})^2}{V_{11}V_{12}}.$$

Consequently, the effective FOV ratio ρ is calculated as

$$\rho = 1 + \frac{(1 - V_{11} + V_{12})^2}{4V_{11}V_{12}}. \quad (21)$$

The case is valid for such direction only if all of the following conditions are satisfied simultaneously:

- $V_{11}V_{12} < 0$, ensuring that ratio ρ remains below or equal to 1;
- $V_{11}^2 + V_{12}^2 < 1$, ensuring that the vector $[V_{11}, V_{12}, V_{13}]$ is a unit vector indicating the direction of corresponding axis;
- $-1 < -(V_{12} + 1)/V_{11} < 1$ and $-1 < (1 - V_{11})/V_{12} < 1$, ensuring that the edges of parallelogram A intersect with those of parallelogram B.

To obtain the range of ρ , values are numerically assigned to V_{11} and V_{12} , each ranging from -1 to 1 with a step of κ . Only values that satisfy the above conditions for the relationship between V_{11} and V_{12} are considered. The ranges of ρ for varying step sizes κ are presented in Table 2. According to the table, the image produced by the TOI may include small missing corner regions, leading to an effective FOV of 91.42% of the full image (worst-case scenario) in the estimation. Astronomers should be aware of this limitation when using TOI.

The findings in this section demonstrate that the TOI successfully reconstructs the celestial sources over the image (with corner caveats as mentioned), while also reducing the noise level in comparison to WSClean.

5.2 Computational performance

During our experiments, FIP-TOI is executed on an NVIDIA H100¹¹. To assess computational efficiency for data generated from various telescope configurations, the TOI processes images of varying sizes, conducting 10 trials per size. By measuring the execution time of the CUDA kernels indicated by the green boxes in Fig. A1 and averaging across all 10 runs, we derive the results presented in Fig. 5.

The results indicate that variations in telescope configurations have little impact on computation time. In our experiments, the Measurement Set for a single time slot contains 130816 baselines for SKA1-LOW, 2080 for SKA AA2, and 1711 for MeerKAT. Despite differences in baseline counts, the visibility gridding for each baseline is handled in parallel. Notably, the computational efficiency of

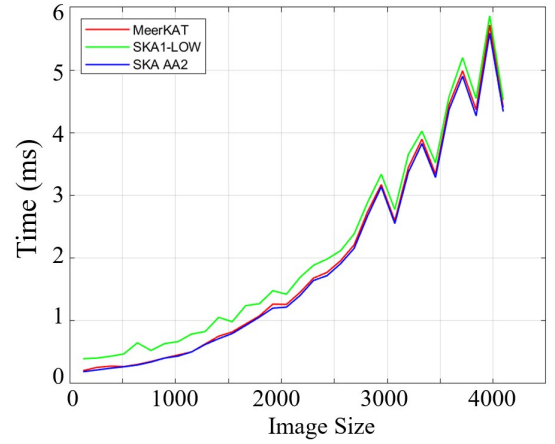


Figure 5. Computation time of kernels in TOI, with image size represented by N pixels.

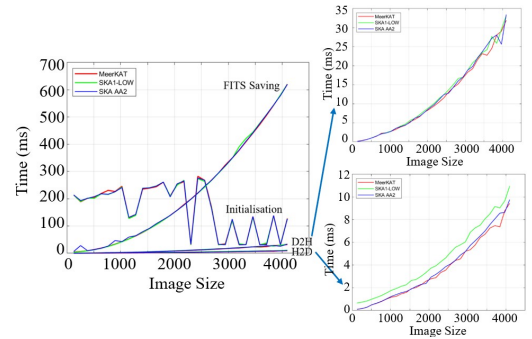


Figure 6. Execution time for initialisation, PCIe host-to-device (H2D), PCIe device-to-host (D2H), and FITS saving in the TOI, with image size represented by N pixels. The red, green, and blue curves illustrate the performance on data simulated for MeerKAT, SKA1-LOW, and SKA AA2, respectively.

the TOI remains unchanged by the range of w , as the process involves only a single FFT applied to the visibility plane.

When running the TOI as a stand-alone imaging tool, concurrent bidirectional transfer can be used. Once data transfer is finalised, the dirty snapshot is stored as an FITS file using the C/C++ interface. The execution time for each operation, averaged over 10 trials, is illustrated in Fig. 6.

When integrated into the FIP, the TOI is directly linked to the FITrig, which takes dirty snapshots as input. This eliminates the need to transfer them (D2H) or save them as FITS files. The conceptual parallel execution timeline for the FIP-TOI is illustrated in Fig. 7, outlining the intended design of the fully parallelised pipeline. The FITrig kernels initiate processing once three consecutive snapshots have been produced by the TOI. At the end of the process, only the tLSI matrix is transferred (D2H). For reference, Fig. 8 illustrates the FITrig's kernel execution time and D2H transfer time for different image sizes. Since the FITrig works solely with pixel intensities, variations in telescope configurations do not impact its computation time.

The average time required to produce a single tLSI matrix with FIP-TOI, based on 10 trials, is presented in Fig. 9 (a). The most time-consuming component of this process is the `cuffftPlan2d`, which is 2-D FFT configuration included in the initialisation. When the TOI produces consecutive snapshots of identical image size and baseline counts, whether as a stand-alone imaging tool or as a component

¹¹ <https://resources.nvidia.com/en-us-tensor-core>

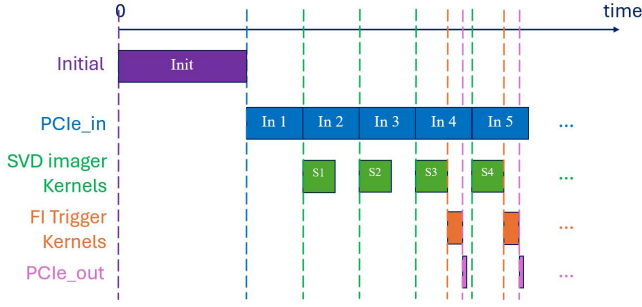


Figure 7. Parallel timeline of the FIP-TOI. The bars in the bottom two rows are too narrow to display labels in the figure.

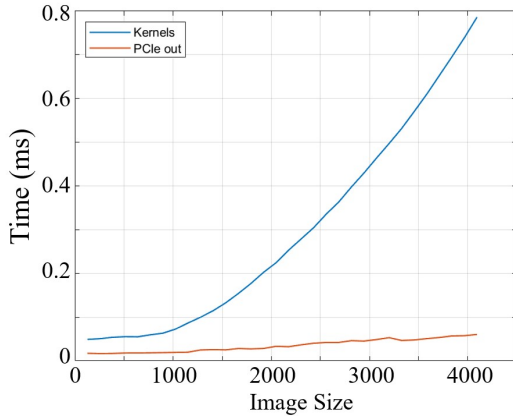


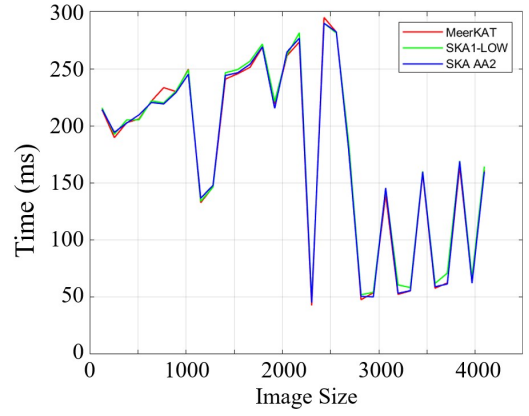
Figure 8. Execution time of the kernels and PCIe D2H within the FITrig, with the image size represented by N pixels.

in the FIP, GPU initialisation procedures such as `cudaMalloc` and `cufftPlan2d` are executed only once at the start. As the number of computed tLSI matrices increases, the effect of initialisation time on each individual computation becomes less significant. Therefore, if we exclude the time spent on `cufftPlan2d`, the remaining computation time for FIP-TOI is illustrated in Fig. 9 (b). As shown, different telescope configurations have minimal influence on the FIP-TOI's computation time.

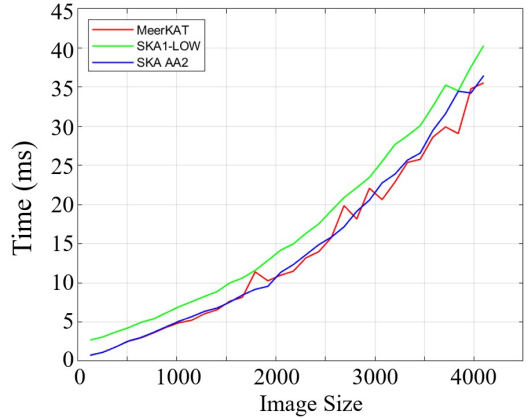
For comparison, we analyse the execution time of the WSClean-based pipeline. Here in this approach, the dirty snapshots produced by WSClean need to be H2D transferred prior to executing the FITrig. WSClean supports multiple gridding methods. In this study, we analyse its performance using both the default w -stacking gridded and the w -snapshot gridded. In experiments utilising the w -stacking gridders, we activate the `-intervals-out` option to enhance WSClean's efficiency by enabling automatic separable computation for each snapshot. Each dataset, generated based on different telescope layouts, consists of ten snapshots. To determine the average processing time per snapshot, we divide the total runtime by 10.

For experiments involving the w -snapshot gridded, WSClean first applies phase rotation to the snapshot data using `chgcentre -minw`, then executes the imaging process while shifting back the phase to the original target. We conduct 10 trials and compute the average time. Interestingly, the TOI performs a comparable phase-shifting operation during the re-projection step. However, our approach implements this within Stream 2 by multi-streaming, as illustrated in Fig. A1, which improves efficiency.

Figure 10 presents a comparison of computation times for the FIP-TOI and WSClean-based pipelines using both the w -stacking and



(a)



(b)

Figure 9. FIP-TOI computation time for data simulated with various telescope configurations, where (a) includes the initialisation time and (b) omits the `cufftPlan2d` time, with image size represented by N pixels.

w -snapshot gridders on datasets simulated with different telescope layouts.

As shown in Fig. 10, WSClean's w -snapshot and per-snapshot implementation of w -stacking exhibit similar performance. However, its performance differs depending on the telescope configuration. This variation arises because different configurations lead to differences in baseline counts and visibility coverage, influencing the required gridding and iFFT operations.

For MeerKAT and SKA AA2, the WSClean-based pipeline processes data more quickly when dealing with smaller images (below approximately $1.8K \times 1.8K$ pixels). In contrast, for larger images exceeding this size, our FIP-TOI outperforms the WSClean-based pipeline. Quantitatively, our FIP-TOI operates considerably faster than the WSClean-based pipeline, delivering speed improvements of 8.80, 11.08, and 10.03 times for $4K \times 4K$ -pixel images produced by datasets from SKA1-LOW, SKA AA2, and MeerKAT telescope configurations, respectively.

5.3 Precision and sensitivity

5.3.1 Performance on GLEAM

To verify the effectiveness of FIP-TOI on datasets with multiple transients, we use OSKAR to simulate three Measurement Sets based on the GLEAM catalogue [Hurley-Walker et al. \(2017\)](#). Each Measurement Set contains visibilities corresponding to a single snap-

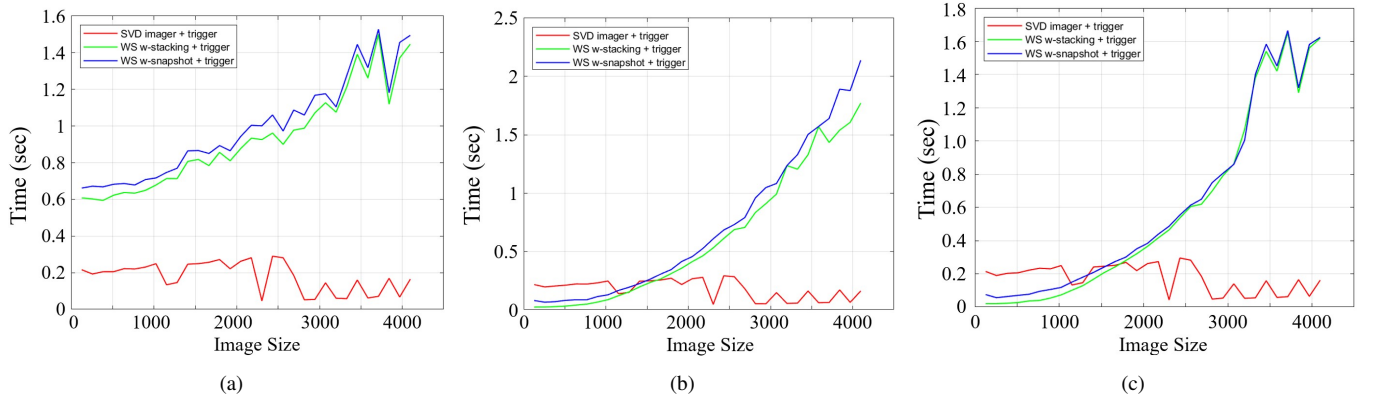


Figure 10. Computation time comparison for the FIP-TOI and WSClean-based pipeline, with results displayed separately for datasets simulated with (a) SKA1-LOW, (b) SKA AA2, and (c) MeerKAT telescope layouts, with image size represented by N pixels.

shot. The first two datasets employ the sky model with sources from “sky2.osm” in Li 2024, while the third dataset employs the sky model with sources from “sky1.osm” in Li 2024. The main difference between the sky models is that the five faintest sources present in sky1 are missing in sky2; these sources are used to represent transients.

Since the GLEAM Catalogue¹² is an extragalactic catalogue observed by the MWA Tingay et al. (2013), an SKA1-LOW precursor, we adopt SKA1-LOW layout in the simulations, with a 1-second dump time Dewdney et al. (2016). The dirty snapshots produced by the WSClean-based pipeline and FIP-TOI are illustrated in Fig. B1 and B2, respectively, with a 1.7-degree FOV. In both figures, the top-row sub-figures are normalised by the largest pixel value across all three dirty snapshots for illustration purposes, while the bottom-row sub-figures are normalised by the largest pixel value of the difference image containing the transients. The colour bars represent the normalised pixel intensities.

While it is rare for 5 transients within the same FOV to vanish simultaneously during real-world observations, this experiment aims to showcase the pipelines’ performance in handling situations with multiple transients in a single FOV. By applying FITrig to the dirty snapshots with $4K \times 4K$ pixels and a tile size of 32×32 pixels Li et al. (2025), tLSI matrices are obtained for both pipelines, as illustrated in Fig. 11. The results demonstrate that both pipelines correctly detect the desired tiles. The flux of the brightest source in the FOV is 0.523 Jy, and the five sources absent have fluxes between 0.030 Jy to 0.046 Jy, making them up to 17.4 times dimmer than the brightest stable source. This experiment highlights the capability of FIP-TOI in detecting multiple faint transients.

5.3.2 Performance on PSR J0901-4046

To verify the performance of FIP-TOI on datasets with a typical on-and-off pulsar, we carry out experiment on the Measurement Set of PSR J0901-4046 collected by MeerKAT, with a dump time of 1.999 seconds.

We begin by restoring snapshots from the Measurement Set using WSClean. The restored (CLEANed) images serve as sky models, which we input into OSKAR to produce a simulated Measurement Set for each snapshot. The simulations employ the same telescope

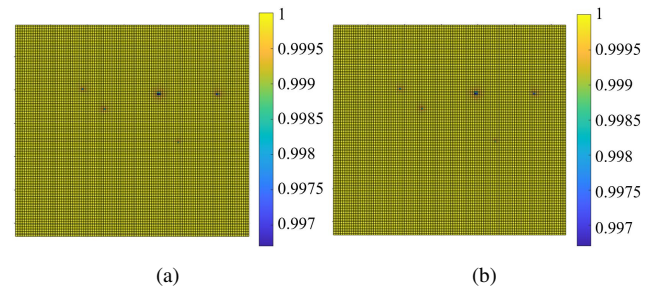


Figure 11. The tLSI matrices for (a) the WSClean-based pipeline (constructed by WSClean + FITrig) and (b) the FIP-TOI (constructed by TOI + FITrig), demonstrating their performance on GLEAM data. The colour bars indicate the tLSI value per tile. The greatest absolute difference that exists between the two matrices is only 3.18×10^{-4} .

configuration as the original dataset. Next, we process these Measurement Sets with both the TOI and the WSClean separately, generating corresponding dirty snapshots. This methodology guarantees that calibration and multi-frequency processing remain consistent across both pipelines, enabling an unbiased comparison.

As examples, dirty snapshots produced by the WSClean-based pipeline and FIP-TOI are illustrated in Fig. B3 and B4, respectively, with a 1.2-degree FOV. In both figures, the top-row sub-figures are normalised by the largest pixel value across three dirty snapshots for illustration purposes, while the bottom-row sub-figures are normalised by the largest pixel value of the difference image containing the pulsar. The colour bars represent the normalised pixel intensities.

In the figures, the pulsar appears solely in the first snapshot, positioned at the image centre. Figure 12 presents enlarged dirty snapshots produced by both pipelines, where the pulsar is visible upon visual inspection.

By applying FITrig to the dirty snapshots with $4K \times 4K$ pixels and a tile size of 32×32 pixels, tLSI matrices are obtained for both pipelines, as illustrated in Fig. 13. The results demonstrate that both pipelines correctly detect the desired tile with similar precision, highlighting the effectiveness of FIP-TOI.

To verify the robustness of FIP-TOI against real-world noise and substantial PSF mismatches, we carry out an “extreme” experiment on the real Measurement Set of PSR J0901-4046. Here, “extreme” refers to using an exceptionally long time difference between snapshots, making the PSF for each snapshot exhibit a significant variation.

¹² <https://heasarc.gsfc.nasa.gov/W3Browse/radio-catalog/gleamegcat.html>

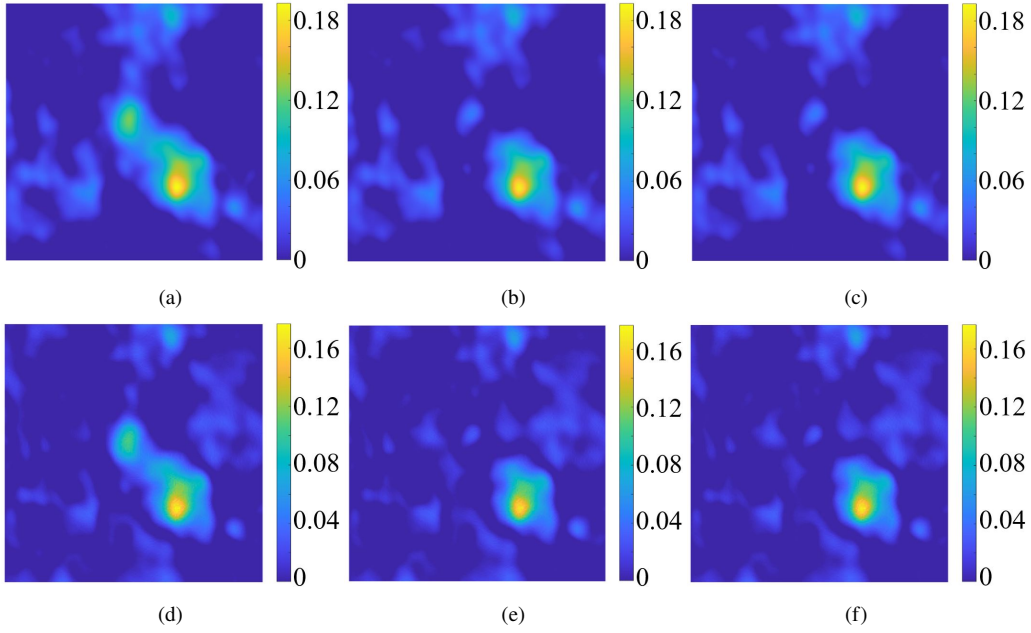


Figure 12. Enlarged dirty snapshots produced by both pipelines, highlighting the area around PSR J0901-4046: the top row showcases snapshots produced using the WSClean-based pipeline, whereas the bottom row presents those produced by FIP-TOI. Each column represents the first, second, and third snapshots in sequence.

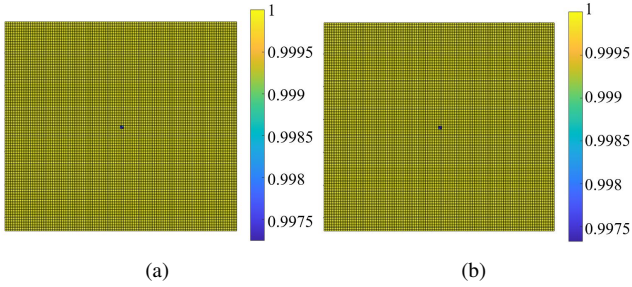


Figure 13. The tLISI matrices for (a) WSClean-based pipeline (constructed by WSClean + FITrig) and (b) the FIP-TOI (constructed by TOI + FITrig), demonstrating their performance on PSR J0901-4046 data. The colour bars indicates the tLISI value per tile. The greatest absolute difference that exists between the two matrices is only 6.79×10^{-4} .

In the experiment, rather than feeding consecutive snapshots into FIP-TOI, we choose three snapshots each separated by a 20-minute gap. Practically, the sampling interval is much shorter than 20 minutes in transient detection. Thus, if FIP-TOI is effective under this condition, it can be expected to perform reliably in practical detection applications.

Figure 14 (a) illustrates the z-score results for detection using the 20-minute intervals on the real data. For comparison, Fig. 14 (b) displays the z-score results for detection on simulated data, with the corresponding tLISI output provided in Fig. 13 (b). While Fig. 14 indicates that real data exhibits higher noise levels, as reflected in the z-score distribution, the noise does not impede successful detection. The z-scores for the pulsar tiles are 54.56 in real data and 68.77 in simulated data, both surpassing the detection threshold of $\tau = 6$ Li et al. (2025), meaning that the pulsar is detected in both cases, demonstrating the robustness of FIP-TOI even under significant PSF mismatches caused by long sampling intervals and realistic noise conditions.

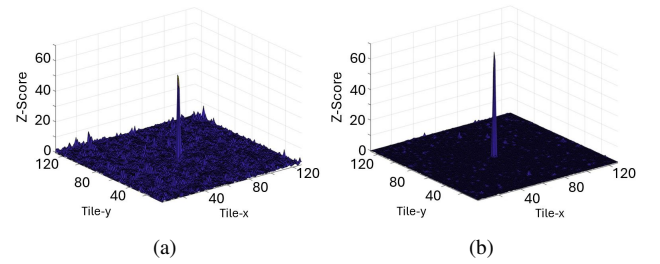


Figure 14. Z-score results of FIP-TOI for datasets containing PSR J0901-4046: (a) displays results from real data with input snapshots spaced 20 minutes apart, while (b) presents the corresponding z-score results related to Fig. 13 (b).

5.3.3 Performance on PSR J1703-4902

In contrast to PSR J0901-4046, which shows an on-and-off pattern throughout the observation, PSR J1703-4902¹³ Driessen et al. (2022); Tremou et al. (2020) exhibits a gradual variation in brightness over time, as depicted in Fig. 15. This figure is derived by recording the peak pixel intensity of PSR J1703-4902 in each restored snapshot (within a 1.0-degree FOV), deconvolved using WSClean. The observation was carried out with MeerKAT, employing a 7.9966-second dump time. Although the pulsar intensity fluctuates, FIP-TOI remains capable of detecting these variations.

To ensure an unbiased comparison between the two pipelines while maintaining consistency in calibration approach and multi-frequency processing, we conduct simulations by supplying OSKAR with sky models that include the positions and fluxes of sources within the

¹³ <https://simbad.cds.unistra.fr/simbad/sim-id?bibyear1=1850&bibyear2=%24currentYear&submit=Display&Ident=%403509446&Name=PSR+J1703-4902&bibdisplay=refsum&bibyear1=1850&bibyear2=%24currentYear>

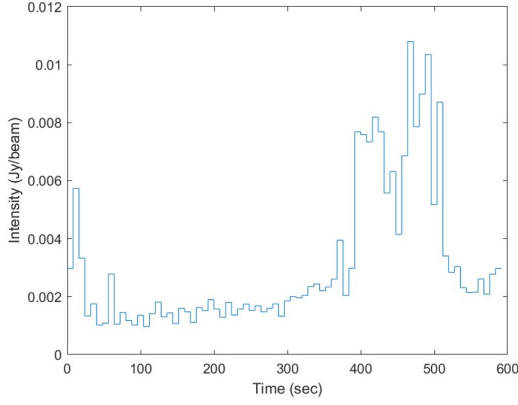


Figure 15. Intensity fluctuation of PSR J1703-4902 in the measurement.

targeted FOV. This approach ensures that the pulsar’s intensity variations in the simulation align with those collected in the real measurement. As examples, Fig. 16 presents a dirty snapshot where the pulsar is perceptible to the Human Visual System (HVS) for each pipeline. The intensity scales in both sub-figures are normalised for illustration purposes, with colour bars representing the normalised pixel intensities. The images are $4K \times 4K$ pixels in size, where the cell size is set to 0.000245 degrees.

Figure 17 displays enlarged dirty snapshots, with the pulsar easily identifiable through visual inspection.

We apply FITrig to the reconstructed dirty snapshots, using 32×32 -pixel tiles, resulting in a tLISI cube for each pipeline. This cube has two dimensions for tile indices and a third dimension representing the snapshot index (which corresponds to time). We then accumulate the data along the time dimension to form a matrix that summarises the overall changes. We calculate the z score Li et al. (2025) for this accumulated matrix using

$$z_t = \frac{(1 - t\hat{L}\hat{S}I_t) - (1 - \mu)}{\sigma} = \frac{\mu - t\hat{L}\hat{S}I_t}{\sigma}, \quad (22)$$

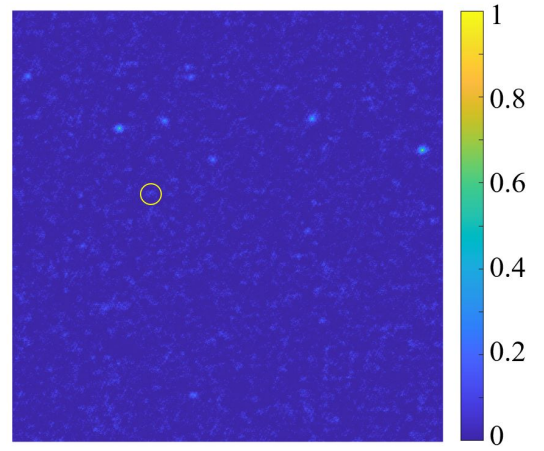
where $t\hat{L}\hat{S}I$ represents the accumulated tLISI matrix, t indicates tile index, μ and σ represent mean and standard deviation, and z indicates the z score. We then keep only the values that exceed the threshold of $\tau = 6$. This results in the matrices presented in Fig. 18 (a) for the WSClean-based pipeline and (b) for FIP-TOI.

The results show that both pipelines correctly detect the desired tile. However, the WSClean-based pipeline generates more false positives, though these generally have low significance. In contrast, FIP-TOI produces fewer false positives, but some of these are highly significant. Determining the true transient from the pipelines’ candidate outputs is not within the scope of this study and will be explored in future work.

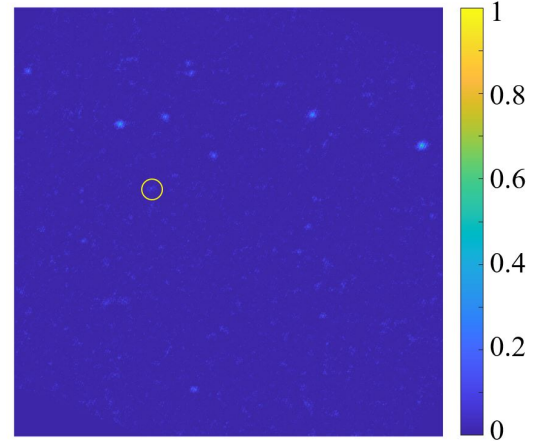
6 CONCLUSION

In this work, we propose the TOI, an innovative wide-field imaging technique for fast and accurate transient detection. TOI addresses key limitations in existing approaches by improving image quality, computational performance, and robustness of FIP across diverse observational scenarios. The key contributions include:

- **Novel imaging formulation:** TOI is built upon the van Cittert-Zernike theorem-based visibility equation and its vector-based predecessor, leveraging multi-variable calculus, linear algebra, and trigonometry to ensure precise and robust imaging.

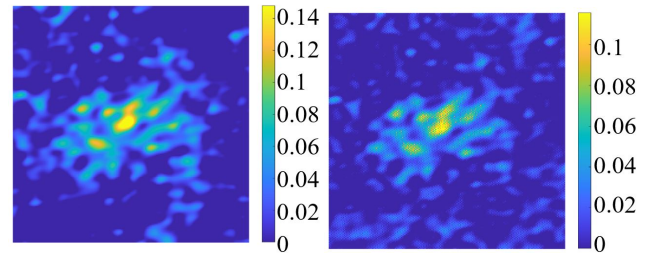


(a)

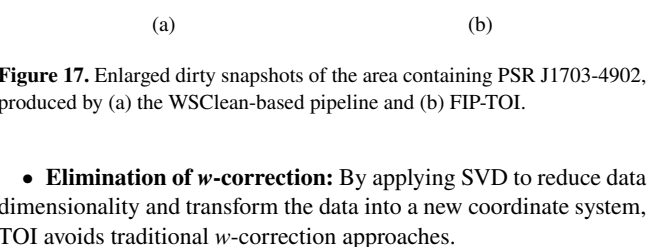


(b)

Figure 16. Dirty snapshots showing PSR J1703-4902, visible to the HVS, reconstructed with (a) the WSClean-based pipeline and (b) FIP-TOI. The pulsar is marked with yellow circles.



(a)



(b)

Figure 17. Enlarged dirty snapshots of the area containing PSR J1703-4902, produced by (a) the WSClean-based pipeline and (b) FIP-TOI.

- **Elimination of w -correction:** By applying SVD to reduce data dimensionality and transform the data into a new coordinate system, TOI avoids traditional w -correction approaches.

- **Fully custom, GPU-accelerated implementation:** TOI is implemented using CUDA and leverages high-performance GPU parallel programming. By utilising a multi-streaming strategy with stream synchronisation and event management, it reduces blocking and enhances concurrency. In contrast to existing imagers, TOI is implemented by custom-developed functions based on our mathematical

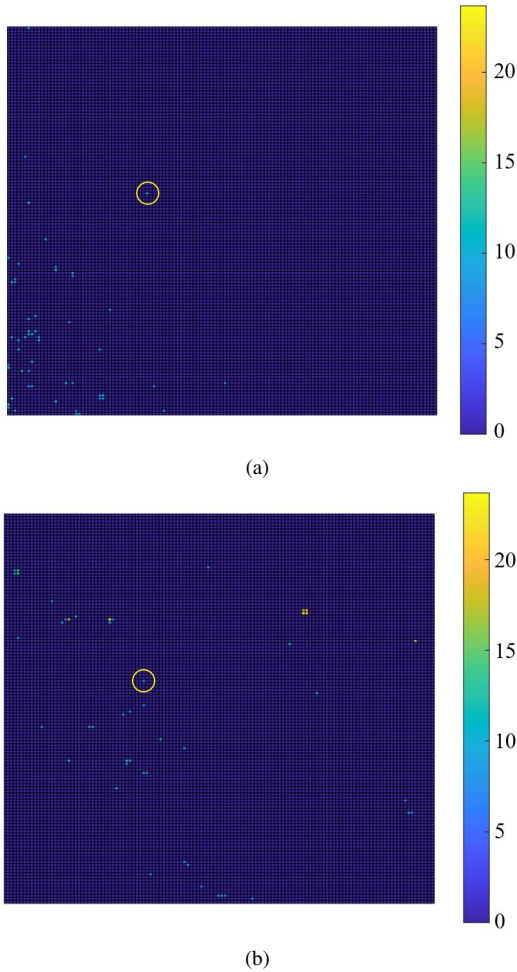


Figure 18. Z-score matrices after thresholding for (a) the WSClean-based pipeline (constructed by WSClean + FITrig) and (b) FIP-TOI (constructed by TOI + FITrig), demonstrating their performance on data with PSR J1703-4902. The colour bars represent the thresholded z scores per tile. In each sub-figure, the pulsar tile is marked with a yellow circle.

framework shown in Section 3, removing the need for third-party libraries like WCSLIB or Nifty Gridder.

- **Integration into a full detection pipeline, FIP-TOI:** We combine TOI (imager) with FITrig (source finder) to build the end-to-end, real-time FIP-TOI transient detection pipeline.

The results show that TOI reconstructs celestial sources with high accuracy and effective noise suppression, outperforming existing imagers such as WSClean in both reconstruction quality and computational efficiency. When operating independently, the TOI achieves remarkable processing speeds — reconstructing a $4K \times 4K$ -pixel image in about 4.5 milliseconds of CUDA kernel execution under GPU acceleration. Integrated into the FIP, this enables a 10-fold speedup compared to the conventional WSClean-based approach, establishing our method as a superior solution for high-performance transient detection.

The FIP-TOI’s capability is verified by its adaptability across various observational scenarios, including an FOV containing multiple transients, a pulsar with on-and-off behaviour, and a pulsar showing gradual intensity variations throughout the observations. These results show the pipeline’s robustness in processing diverse datasets while enabling timely detection of transient events.

FIP-TOI has resulted in a highly advanced tool that enhances telescope data processing, greatly improving both efficiency and accuracy. Time-domain approaches often struggle to accurately localise transients during detection. In contrast, the image-based FIP provides precise transient localisation, offering a significant edge in studying transients. Moreover, FIP-TOI is able to detect long-period pulsars (as demonstrated in Section 5.3.2 for the pulsar with a 75.9-second period), which remain challenging to detect using conventional time-domain methods.

In summary, FIP-TOI, equipped with a custom-developed image-based detection system and the real-time processing capability, enables timely and highly accurate multi-spectral follow-up observations. This makes it a crucial tool for detecting transients with next-generation telescopes, enhancing the overall scientific yield.

ACKNOWLEDGEMENTS

The authors acknowledge support from STFC Grant (ST/W001969/1). The authors acknowledge the use of the University of Oxford Advanced Research Computing (ARC; Richards 2015) facility in carrying out this work. Special thanks are extended to Ian Heywood for supporting the data of PSR J0901-4046 and to Rob Fender and Joe Bright for supporting the data of PSR J1703-4902. The authors are particularly grateful to Ali Taqi for helpful discussions on projection. Gratitude is extended to Fred Dulwich and Ben Mort for valuable guidance on OSKAR. The authors also express sincere thanks to Feng Wang and Yangfan Xie for their insightful discussions on *ws-snapshot*. The authors are especially grateful to Mark Calabretta, Francois-Xavier Pineau, and Matthieu Baumann for helpful discussions on re-projection and WCSLIB. The authors’ heartfelt thanks go to André Offringa for the enlightening discussions on WSClean.

DATA AVAILABILITY

Data supporting the findings of this study are available from the corresponding author upon request.

REFERENCES

- Burke B., Graham-Smith F., Wilkinson P., 2019, *An Introduction to Radio Astronomy*, 4 edn. Cambridge University Press, Cambridge
- Calabretta, M. R. Greisen, E. W. 2002, *A&A*, 395, 1077
- Caleb M., Heywood I., Rajwade K., et al., 2022, *Nat Astron*, 6, 828
- Cornwell T., Perley R., 1992, *A&A*, 261, 353
- Cornwell T., Golap K., Bhatnagar S., 2008, *IEEE J. Sel. Topics Signal Process.*, 2, 647
- Cornwell T., Voronkov M., Humphreys B., 2012, in Bones P., Fiddy M., Millane R., eds, *Image Reconstruction from Incomplete Data VII*. SPIE
- Dewdney P., Wagg J., Braun R., Turner W., 2016, *SKA1-LOW Configuration - Constraints & Performance Analysis*, https://www.skao.int/sites/default/files/documents/d17-SKA-TEL-SKO-0000557_01-DesignConstraints-1.pdf
- Driessen L. N., Stappers B. W., Tremou E., et al., 2022, *Mon. Not. R. Astron. Soc.*, 512, 5037
- Dulwich F., Mort B., Stolyarov V., et al., 2022, *OxfordSKA/OSKAR*, doi:10.5281/zenodo.5722575
- Greisen, E. W. Calabretta, M. R. 2002, *A&A*, 395, 1061
- Hancock P. J., Murphy T., Gaensler B. M., et al., 2012, *Mon. Not. R. Astron. Soc.*, 422, 1812
- Hancock P. J., Trott C. M., Hurley-Walker N., 2018, *Publ. Astron. Soc. Aust.*, 35, e011

Hopkins A. M., Miller C. J., Connolly A. J., et al., 2002, *AJ*, 123, 1086

Humphreys B., Cornwell T., 2011, *SKA MEMO*, 132

Hurley-Walker N., Callingham J., Hancock P., et al., 2017, *MNRAS*, 464, 1146

Kent J., Dowell J., Beardsley A., Thyagarajan N., Taylor G., Bowman J., 2019, *Monthly Notices of the Royal Astronomical Society*, 486, 5052

Kirk D., 2007, in *Proceedings of the 6th International Symposium on Memory Management*. pp 103–104

Law C. J., Bower G. C., Burke-Spolaor S., et al., 2018, *The Astrophysical Journal Supplement Series*, 236, 8

Li X., 2024, *Sky Models*, doi:10.5281/zenodo.14744218

Li X., Adámek K., Armour W., 2023, *SoftwareX*, 23, 101500

Li X., Adámek K., Armour W., 2024a, in *Astronomical Data Analysis Software and Systems (ADASS) XXXIV*.

Li X., Adámek K., Armour W., 2024b, *ApJS*, 274, 37

Li X., Adámek K., Armour W., 2025, *A&C*

Lorimer D., Kramer M., 2004, *Handbook of Pulsar Astronomy*. Cambridge Observing Handbooks for Research Astronomers, Cambridge University Press

McMullin J., Waters B., Schiebel D., Young W., Golap K., 2007, in Shaw R., Hill F., Bell D., eds, Vol. 376, *Astronomical Data Analysis Software and Systems XVI*. ASP Conference Series, pp 127–130

Murdin P., Murdin L., 2011, *Supernovae*, 2nd edn. Cambridge University Press

Murphy T., Kaplan D. L., Stewart A. J., et al., 2021, *Publications of the Astronomical Society of Australia*, 38, e054

Offringa A., et al., 2014, *Mon. Not. R. Astron. Soc.*, 444, 606

Pelisoli I., Marsh T., Buckley D., et al., 2023, *Nat Astron*, 7, 931

Perley R., 1999, in Taylor G., Carilli C., Perley R., eds, Vol. 180, *Synthesis Imaging in Radio Astronomy II*. Astronomical Society of the Pacific Conference Series, pp 383–400

Popov S. B., Postnov K. A., Pshirkov M. S., 2018, *Physics-Uspekhi*, 61, 965

Richards A., 2015, *University of Oxford Advanced Research Computing*, doi:10.5281/zenodo.22558

Selig M., Bell M. R., Junklewitz H., Oppermann N., Reinecke M., Greiner M., Pachajoa C., EnBlin T. A., 2013, *A&A*, 554, A26

Serra P., Westmeier T., Giese N., et al., 2015, *Mon. Not. R. Astron. Soc.*, 448, 1922

Sokolowski M., Aniruddha G., Pietrantonio C. D., Harris C., Price D. C., McSweeney S., Wayth R. B., Bhat N. D. R., 2024, *High-time resolution GPU imager for FRB searches at low radio frequencies (arXiv:2405.13478)*, <https://arxiv.org/abs/2405.13478>

Stolyarov V., Li X., Heywood I., Adamek K., 2025, in *HEASA. PoS*

Swart G., et al., 2024, in Marshall H. K., Spyromilio J., Usuda T., eds, Vol. 13094, *Ground-based and Airborne Telescopes X*. SPIE, p. 130940L

The CASA Team 2021, *CASA Fundamentals*, <https://casadocs.readthedocs.io/en/latest/notebooks/casa-fundamentals.html>

The CASA Team et al., 2022, *Publications of the Astronomical Society of the Pacific*, 134

Thompson A., 1999, in Taylor G., Carilli C., Perley R., eds, Vol. 180, *Synthesis Imaging in Radio Astronomy II*. Astronomical Society of the Pacific Conference Series, pp 11–36

Thompson A. R., Moran J. M., Swenson G. W., 2017, *Van Cittert–Zernike Theorem, Spatial Coherence, and Scattering*. Springer International Publishing, Cham, pp 767–786

Tingay S. J., Goeke R., Bowman J. D., et al., 2013, *Publ. Astron. Soc. Aust.*, 30, e007

Tremou E., Corbel S., Fender R. P., et al., 2020, *Mon. Not. R. Astron. Soc.: Letters*, 493, L132

Westmeier T., Kitaëff S., Pallot D., et al., 2021, *Mon. Not. R. Astron. Soc.*, 506, 3962

Woudt P., Fender R., Corbel S., et al., 2018, in *MeerKAT Science: On the Pathway to the SKA (MeerKAT2016)*. PoS, doi:10.22323/1.277.0013

Xie Y.-F., et al., 2022, *Monthly Notices of the Royal Astronomical Society*, 515, 1973

Ye H., Gull S. F., Tan S. M., Nikolic B., 2019, *Monthly Notices of the Royal Astronomical Society*, 491, 1146

Ye H., Gull S., Tan S., Nikolic B., 2021a, *High dynamic range wide field imaging method in radio interferometry*, <https://www.semanticscholar.org/paper/High-dynamic-range-wide-field-imaging-method-in-Ye-Gull/20b41c3d4e9eb2ace3911780bfa78a57071fb9ff>

Ye H., Gull S. F., Tan S. M., Nikolic B., 2021b, *Monthly Notices of the Royal Astronomical Society*, 510, 4110

APPENDIX A: GPU IMPLEMENTATION AND FUNCTIONAL FLOW

APPENDIX B: DIRTY SNAPSHOTS PRODUCED BY WSCLEAN-BASED PIPELINE AND FIP-TOI

This paper has been typeset from a \LaTeX file prepared by the author.

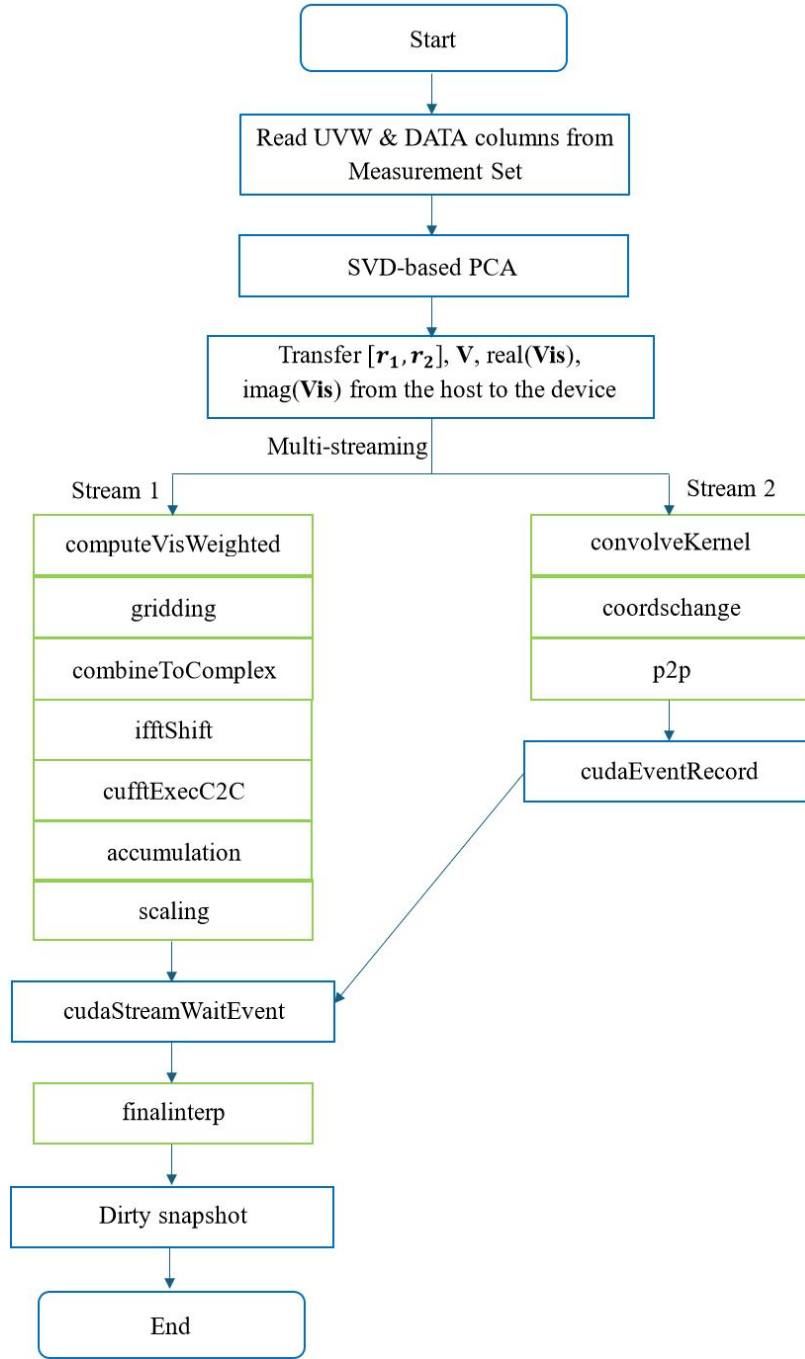


Figure A1. Flowchart of TOI, with green operations indicating CUDA kernels.

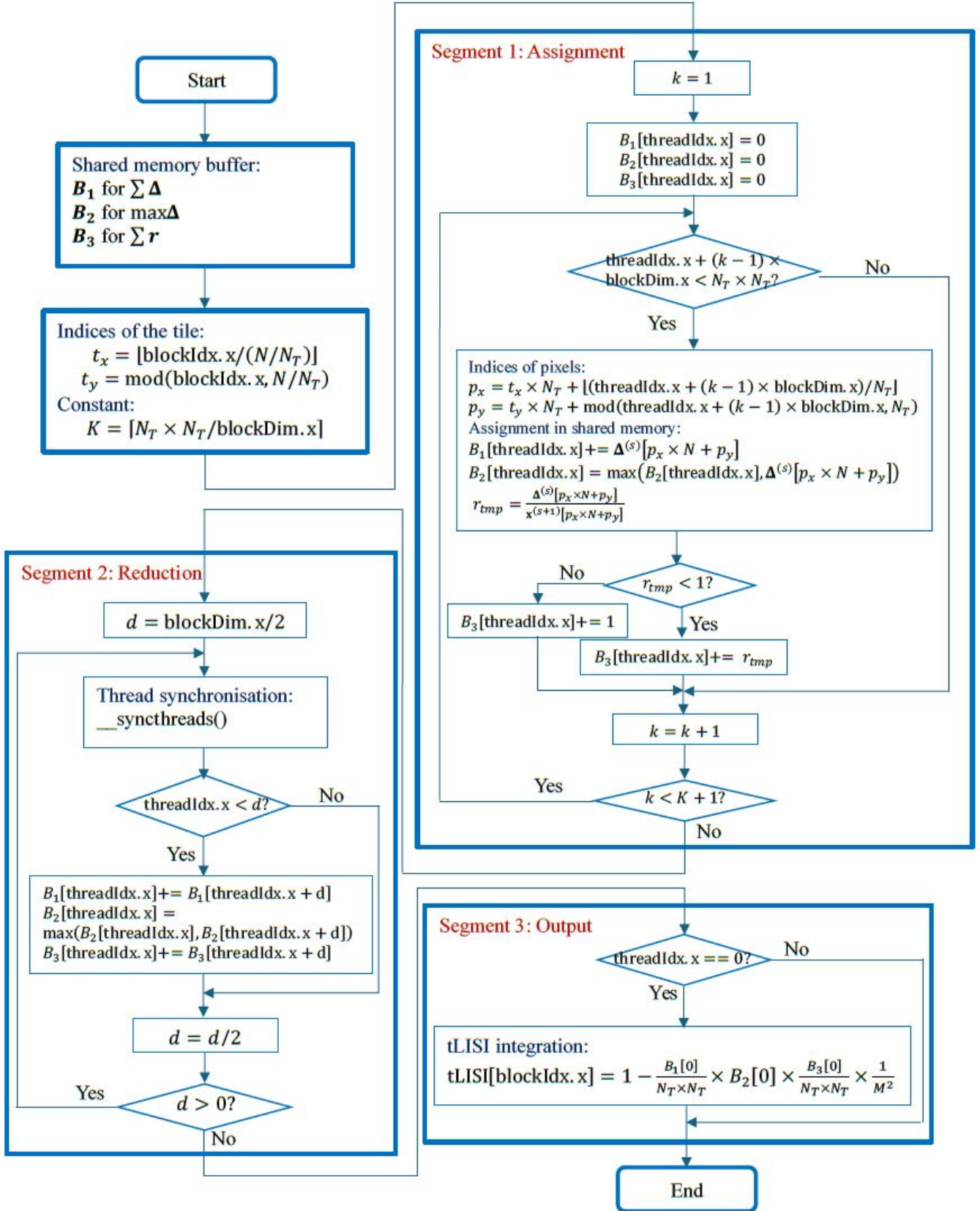


Figure A2. Functional block diagram of tLISI kernel in FITrig.

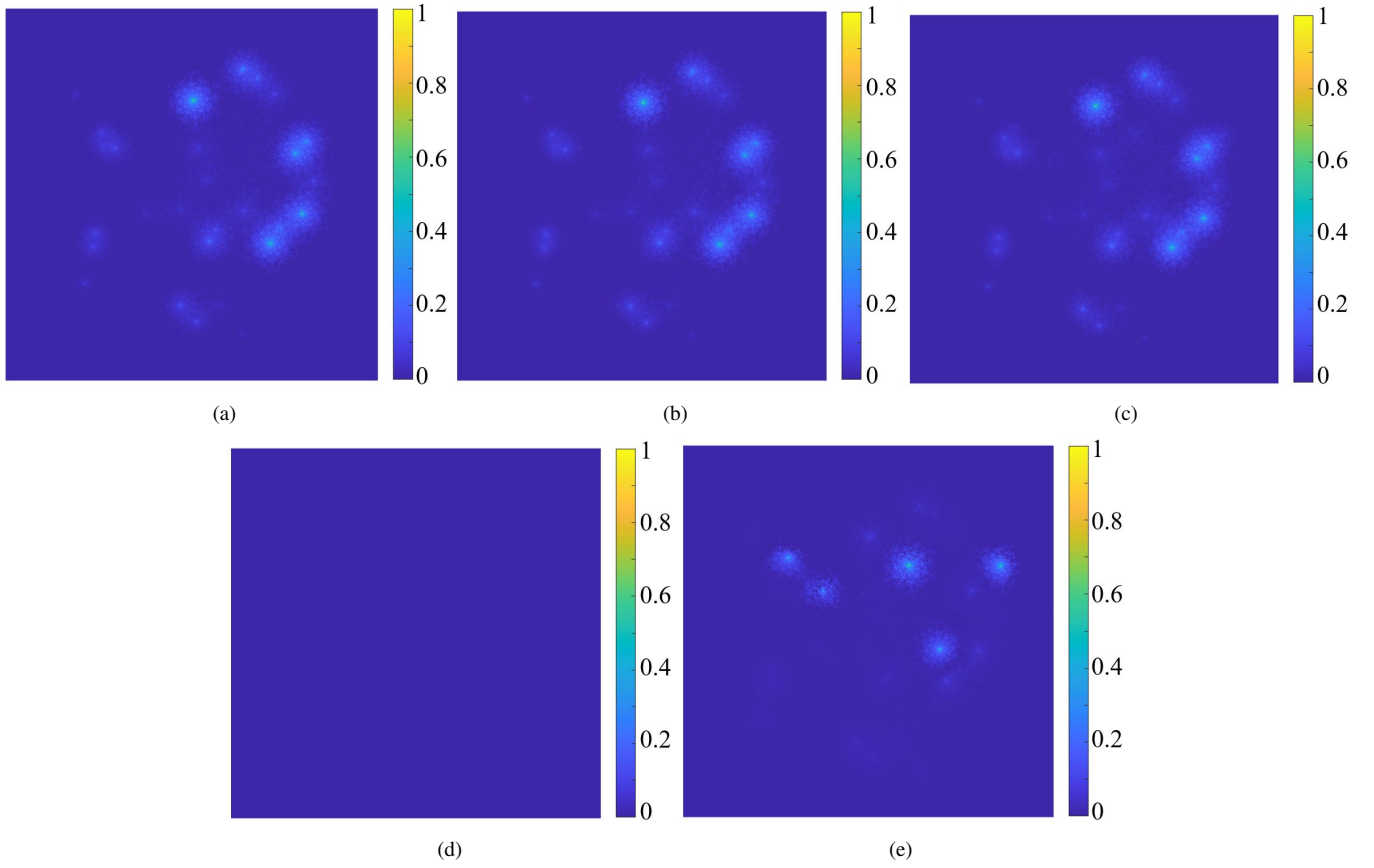


Figure B1. Three dirty snapshots of GLEAM produced by the WSClean-based pipeline: the (a) first, (b) second, and (c) third snapshots are presented in the top row. In the bottom row, the difference images are shown: the difference (d) between the first and second snapshots, and (e) between the second and third snapshots.

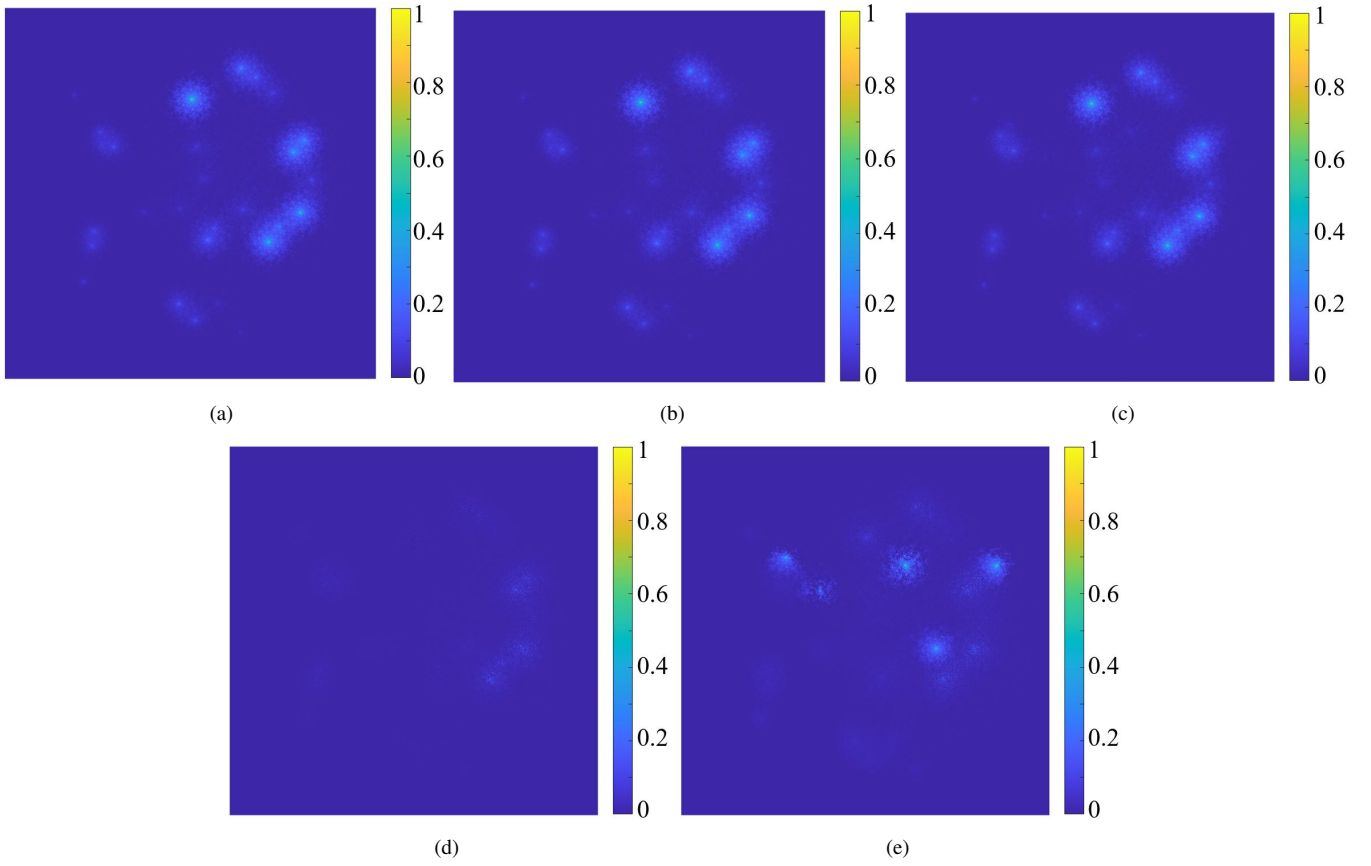


Figure B2. Three dirty snapshots of GLEAM produced by FIP-TOI: the (a) first, (b) second, and (c) third snapshots are presented in the top row. In the bottom row, the difference images are shown: the difference (d) between the first and second snapshots, and (e) between the second and third snapshots.

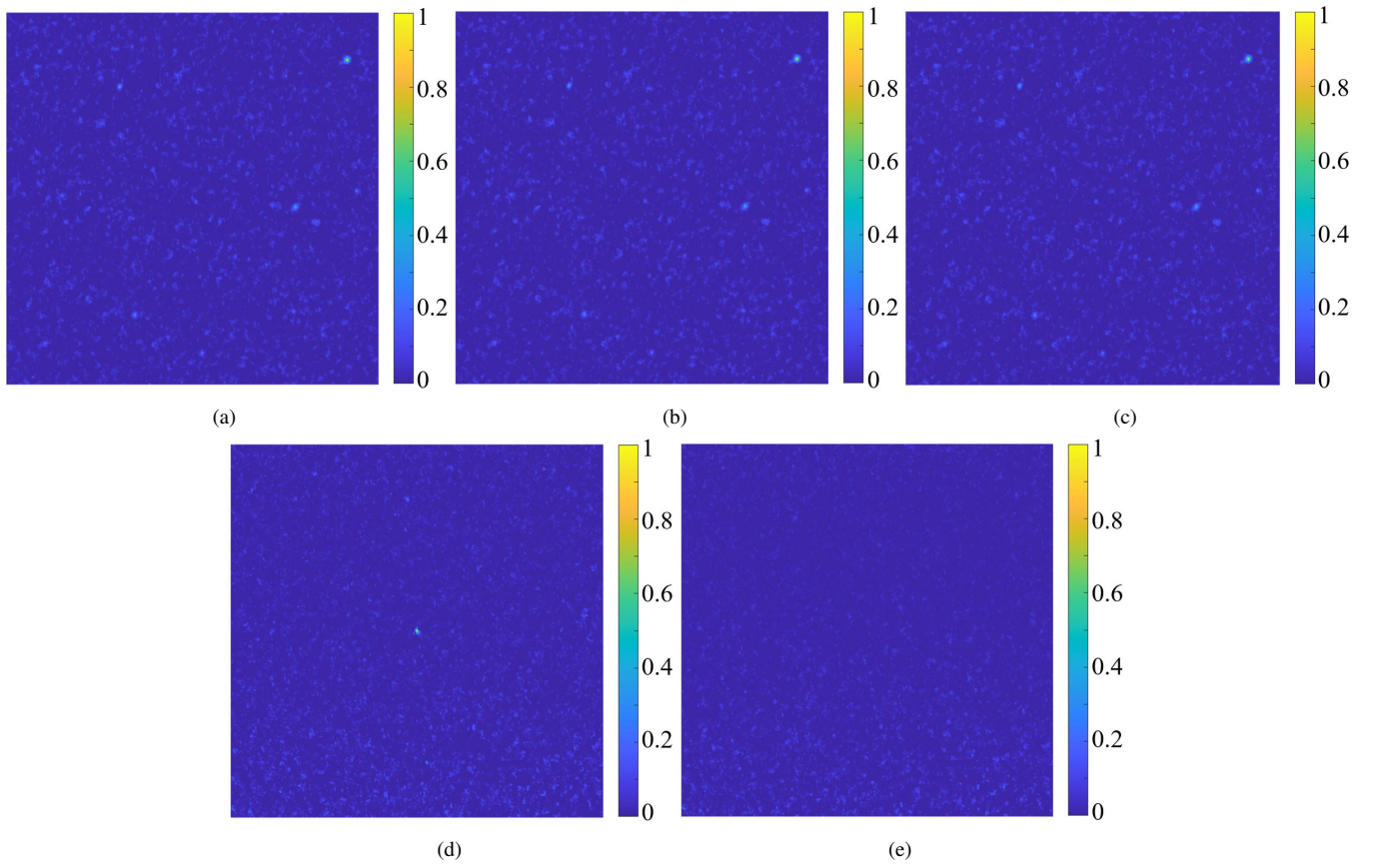


Figure B3. Three dirty snapshots containing PSR J0901-4046 produced by the WSClean-based pipeline: the (a) first, (b) second, and (c) third snapshots are presented in the top row. Below, the difference images are shown: the difference (d) between the first and second snapshots, and (e) between the second and third snapshots.

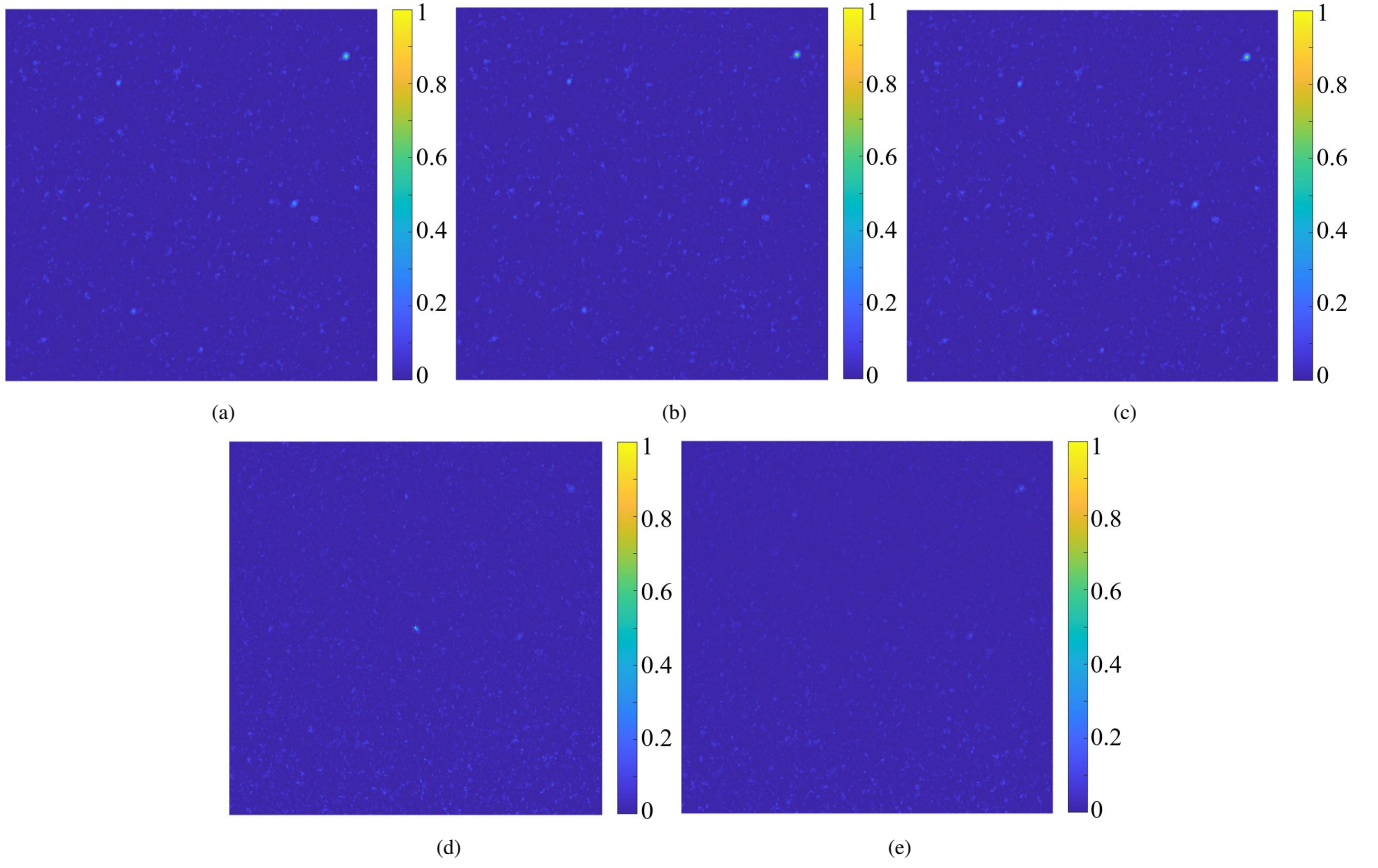


Figure B4. Three dirty snapshots containing PSR J0901-4046 produced by FIP-TOI: the (a) first, (b) second, and (c) third snapshots are presented in the top row. Below, the difference images are shown: the difference (d) between the first and second snapshots, and (e) between the second and third snapshots.